A seasonal study of mesospheric temperatures and emission intensities at Adelaide and Alice Springs

L. J. Gelinas, J. H. Hecht, and R. L. Walterscheid,
Space Science Applications Laboratory,
The Aerospace Corporation,
M2-260, P. O. Box 92957,
Los Angeles, CA 90009.

R.G. Roble, High Altitude Observatory
National Center for Atmospheric Research
Box 3000
Boulder, CO 80307-3000

J. Woithe,
Department of Physics and Mathematical Physics,
University of Adelaide, Adelaide 5005 SA Australia.

Abstract

Aerospace imagers operating at Alice Springs (23°42’ S, 133°53’ E) and Adelaide (34°55’S, 138°36’ E) have collected more than four years of OH and O_2 atmospheric emission data. Images were taken over the course of each moonless night at 5-minute intervals and used to determine OH Meinel (6,2) and O_2 Atmospheric (0,1) band emission intensities and temperatures, as well as atmospheric gravity wave parameters. The NCAR general circulation model TIME-GCM was run for years 2002-2005 for comparison with these data.

The data presented here show the interannual variability of OH and O2A emissions at two sites, Alice Springs and Adelaide, over a 4-year period. It was found that the TIME-GCM successfully reproduces many features observed in the data, particularly the equinoctial signatures associated with the diurnal tide. Several discrepancies noted between the observations and the model may be attributed to an inadequate model specification of the seasonal variation of gravity waves, which are shown to be correlated with the strength of solstice minima. The model also successfully described many of the mesospheric changes observed during the 2002 stratospheric warming event.

1 Introduction

The 80 to 100 km altitude regime, commonly known as the mesosphere and lower thermosphere (MALT), is a region largely controlled by tides and gravity waves. The propagation and dissipation of these waves in the MALT region generates fluctuations and secular variations in density, composition, temperature, and wind structure [e.g. *Lindzen,* 1981; *Holton,* 1983; *Forbes,* 1995; *Roble and Shepherd,* 1997]. These processes can change transport and diffusion characteristics, altering MALT density and temperature profiles and producing airglow intensity variations. Ground-based airglow imagers can be used to measure these density and temperature variations, providing valuable data for the study of MALT processes over a wide range of temporal and spatial scales.

Long-term observations of airglow rotational temperature and intensity are essential to climatological studies, and have been used to characterize the global annual and semiannual oscillations [e.g. *Weins and Weill,* 1973; *Buriti et al.*, 2004]. Ground-based measurements of the OH Meinel band emissions at multiple sites established the latitudinal dependence of the annual and semiannual oscillations [*Weins and Weill,* 1973; *Fukuyama,* 1976; *Fukuyama,* 1977]. The semiannual oscillation dominates at low latitudes, with airglow intensity maxima observed near the equinoxes, and is attributable to a combination of eddy forcing (eastward phase) and advection by the mean meridional circulation [*Andrews et al.*, 1987; *Dunkerton,* 1982]. The eddy forcing which drives the semiannual oscillation has been attributed to breaking gravity waves [*Dunkerton,* 1982]. This semiannual variation diminishes in strength with increasing latitude and is

eventually overtaken by the annual oscillation, which dominates at middle and high latitudes. OH emission intensities associated with the annual oscillation maximize near the winter solstice. The annual oscillation is the result of seasonal reversals in the mean meridional circulation in the upper mesosphere and mesopause region driven by breaking of small-scale gravity waves, which produces strong upward transport and cold summertime temperatures at the mesopause [*LeTexier et al.*, 1987; *Holton*, 1983]. This overall pattern of low-latitude/semiannual and high-latitude/annual behavior has been observed repeatedly in ground-based measurements, including mesospheric O2 atmospheric band emissions and in OH and O2 atmospheric rotational temperatures [e.g., *Takahashi et al.*, 1995; *Clemesha et al.*, 1990; *Taylor et al.*, 2005; *Buriti et al.*, 2004].

Although the basic characteristics of the annual and semiannual variations in the upper mesosphere and lower thermosphere (MALT) have been established, observations often show considerable interannual variability. The effects due to interplay with various modes of oscillation (gravity waves, higher-order tides, non-migrating tides, planetary waves, QBO) and tidal variability are not well understood [*Garcia et al.*, 1997; *McLandress*, 2002, *Orland and Alexander*, 2006]. Coupling between short-period waves and tides and long-term annual and semiannual oscillations produces an interannual variability, although a specific pattern has not been confirmed by measurements [*Vincent et al.*, 1998; *Marsh et al.*, 2006; *Zhang et al.*, 2006; *Shepherd et al.*, 2006]. The (1,1) migrating diurnal tide is the dominant tidal mode at latitudes equatorward of about 30 degrees, having a vertical wavelength of about 25-30 km and breaking between 80-90 km altitude [*Forbes*, 1995]. The propagation of this diurnal tide above 80 km is partly

controlled by gravity waves, which can significantly damp the diurnal tide near the mesopause [*Roble and Shepherd,* 1997; *Fritts,* 1995*; Ortland and Alexander,* 2006*; McLandress et al.*, 2002]. In contrast, the semidiurnal tide is the dominant tidal mode poleward of 30 degree latitude. Several semidiurnal tidal modes pass nearly unattenuated through the mesopause, making it the dominant tide at higher altitudes [*Fuller-Rowell,* 1995]. However, the main migrating semidiurnal tidal mode (2,2) can be attenuated by evanescence in the upper mesosphere [*Walterscheid and Venkateswaran,* 1979].

The dominant annual and semiannual oscillations have been observed to vary greatly from year-to-year, presumably influenced by gravity waves, planetary waves and the quasi-biennial oscillation. High resolution airglow imagers with short exposure times are well-suited to the study of short period atmospheric gravity waves (AGWs) and long period tidal and planetary waves in the MALT region. Increasingly, satellite measurements have also been used to study this variability on a global scale, although the limited temporal resolution often prevents investigation of site-to-site variations or relationship to smaller-scale gravity waves. Characterization of variability in the MALT is essential for complete understanding and modeling, but the task is far from complete. This lack of knowledge is reflected in the predictions of state-of-the–art models such as TIME-GCM [*Roble and Ridley*, 1994]. Although atmospheric chemistry and tidal interactions are well represented in the model, specification of boundary forcing, gravity wave parameterization and other sources of wave-tide interactions or variability are generally poor. The result is that the models, unfortunately, do not explain variability in the MALT region over the full range of time scales.

In this paper, we explore the seasonal and interannual variability of the MALT in long-term airglow measurements at two Australian sites. The data presented here are the result of more than four years of airglow imager observations at Adelaide (34 S) and Alice Springs (23 S). The imagers measure rotational temperature and intensity of two atmospheric emissions, OH Meinel (6, 2) and O2 atmospheric (0, 1). The use of imagers, rather than photometers, also provides information about shorter-period gravity waves, an important driver of seasonal variability. The Adelaide airglow imager is one of several instruments deployed at the site, which also hosts an MF radar and airglow spectrometer, and has been part of several multi-instrument investigations [e.g., *Walterscheid et al.*, 1999; *Hecht et al.*, 1997; *Hecht et al.*, 2001]. The airglow imager stationed at Alice Springs is the only instrument deployed at that site, and provides a complementary tropical site for comparison with mid-latitude Adelaide. The proximity of the two sites on a continent with no significant mountain ranges allows for identification of common climatological features while also providing a means to study mesospheric differences between tropical and middle latitude sites.

The airglow data presented here are compared to results from the NCAR TIME-GCM model. Correlations between the model and data can help identify dominant tidal features in the data, while differences illustrate the effects of wave-induced or location-dependent variations at each site. Model data for each site over the 2002-2005 observation period is analyzed and presented alongside airglow imager data for detailed comparisons. Although the TIME-GCM data successfully reproduces many of the

observed seasonal and tidal features, the considerable interannual variability seen in the observations is not present in the model. Presumably, differences in the observed and predicted interannual variability are due to underestimation of the influence of gravity waves and wave-induced variability in the model. Investigations such as the one described here are therefore essential for guiding model development.

In the following sections we describe the airglow imager instrumentation and the data analysis procedure used to calculate emission intensities and temperatures at each site. Overview data is then presented, followed by harmonic analyses to determine the dominant annual and semiannual oscillations in the temperature and intensity data. These seasonal variations are then considered as a function of local time, an ideal method for illustrating the influence of tidal features and the interannual variability at each site. We conclude with a discussion of dominant features in the data, identifying tidal features that are well-represented by TIME-GCM and pointing out where local or wave-induced variability dominates the seasonal behavior.

2 Experimental Instrumentation and Technique

2.1 Airglow Imagers

Aerospace airglow imagers operating at Alice Springs (23°42’ S, 133°53’ E) and Adelaide (34°55’S, 138°36’ E) have collected more than four years of OH and O_2 atmospheric emission data. Each imager employs five filters covering two rotational lines of the OH Meinel (6,2) emission, two rotational lines of the O2 atmospheric (0,1) emission and a background emission. The exposure time for each filter is 60 seconds. A

full set of measurements is taken every seven minutes and includes two background images and a dark image. The field-of-view of the imager is approximately 46x69 degrees, projected on to a 192 X 128 pixel image. OH temperature is determined by the ratio of the 840.0 nm to 843.0 nm rotation lines, and O2 atmospheric temperature by the ratio of 866.0 nm to 868.0 nm lines [e.g., *Hecht et al.*, 1994: *Hecht et al.*, 1997; *Hecht et al.*, 2004].

The Alice Springs airglow imager was deployed to the site in late 2001 and has been operating nearly continuously through early 2006. Data gaps in early 2002 and mid-2003 correspond to brief maintenance periods. The Adelaide imager was deployed in early 2000, but temperature and intensity data from the first year of operation are unreliable due to amplifier problems. After repair in 2001, the imager operated nearly continuously until it was re-deployed to Darwin, Australia in late 2005.

Degradation of imager performance during long-term operation tends to introduce artificial trends into the airglow data. In order to correct for changes in imager operation over the entire observation period, emission intensities of several guide stars were monitored throughout the period and used to correct the raw data. On average, guide star intensity decreased by approximately 6% between 2001 and 2006. The star correction factor was used to remove artificial trends in temperature and intensity measurements and to verify continuity of imager characteristics before and after maintenance periods.

Subsequent image processing included median filtering to remove the background star field, subtraction of background, and flat-fielding of the image. However, some contamination from the Milky Way was not removed during this preliminary image processing, possibly due to strong Milky Way emissions within the passband of the background filter. For the purpose of image-averaged temperature and intensity determination, the residual Milky Way contamination was removed by calculating the average intensity in each quadrant of the image. Since the signature of Milky Way contamination is clearly evident in both the quadrant-averaged background and quadrant-averaged images, a second background subtraction from the quadrant-averaged image intensity adequately removes the contamination. Milky Way contamination removal was further verified by comparing the average of the four image quadrants to the median of the four quadrants.

Image-averaged temperature and intensity values for each emission at each site were calculated from ratios of the rotational lines, which were then converted to temperature and intensity. Temperatures calculated using this technique and for these filters had not been previously validated by cross-calibration with lidar data. Thus some uncertainty remained as to the absolute temperatures, making comparisons between sites difficult. A common calibration source was found using data from the SABER instrument on NASA's TIMED satellite. Kinetic temperature profiles for overpasses of TIMED/SABER (v1.06) were used to calibrate OH and O_2 atmospheric temperatures at each site. TIMED/SABER OH temperatures were calculated by weighting the kinetic temperature profile with the SABER OH emission profile. The O_2 atmospheric emission was determined by assuming a Gaussian layer profile centered at 94 km with 7 km

FWHM [*McDade*, 1998]. The calculated SABER temperatures were then converted to filter ratios, using the reverse of the process used for image processing. The mean SABER "filter ratio" was calculated for the period 2002-2006 and compared with the observed mean filter ratio for the same period. A multiplicative scaling factor was calculated for each emission temperature (OH and O2A), and ground-based temperature and intensity data recalculated using the scaled filter ratios. The single scaling factor method prevents introduction of artificial long-term trends into the data. The filter ratio scaling factors used for correction of Alice Springs emission data were 1.085 and 1.068 for OH and O2, respectively; scaling factors at Adelaide were 1.038 and 1.165 for OH and O2. The correction factors raised the originally derived average OH temperatures by about 20 degrees at Alice Springs and 10 degrees at Adelaide. Since the O2 temperature is inversely proportional to the O2 filter ratio, the correction factors led to a 5-degree decrease in O2 temperature at Alice Springs and a 10-degree decrease in O2 temperature at Adelaide. As noted in a later section, this correction for O2 temperatures may not be needed. However, while the SABER correction does not guarantee accurate absolute temperatures, the correction does allow for more accurate comparison of temperature variations between sites.

2.2 TIME-GCM

The NCAR TIME-GCM, described in detail by Roble and Ridley (1994), is a three-dimensional, time-dependent model of the Earth's upper atmospheric with horizontal resolution of 5 degrees in both latitude and longitude. The model extends from 30 km to 500 km with a vertical resolution of 2 grid points per scale height, and 5 minute time steps [*Liu and Roble*, 2002]. National Center for Environmental Prediction data provides

lower boundary forcing at 30 km, including 5 and 15 day planetary waves; the 2-day wave is suppressed at the boundary. A seasonally uniform parameterization of gravity waves is used to produce tidal damping.

Full-year runs of TIME-GCM were performed for each site over the 2002-2005 period of observation. Average model temperatures are generally consistent with the ground-based measurements presented here, although amplitudes of the nightly temperature variations are larger in the airglow data. Modeled absolute airglow intensities differ from the observed OH and O2A emission intensities by factors of ~1.5 and ~10, respectively. The source of these discrepancies is related to characteristics of the cross sections used by the model, and that the imagers measure the O2A (0,1) emission while the model determines the intensity of the O2A (0,0) emission. Therefore, to facilitate comparisons between the model and observations, the modeled intensities were scaled to the mean of the observed intensities for both sites.

3 Data presentation and analysis

An overview of the nightly mean emission temperatures at Alice Springs and Adelaide is presented in Figure 1. The temperature data displayed here has been calibrated with respect to TIMED/SABER measurements, as described previously in Section 2, and is shown in black in Figure 1. TIMED/SABER overpass data used in the calibration are shown in blue for each site. Data gaps correspond to cloudy periods or when the imager was inoperative.

OH emission temperature data from Alice Springs and Adelaide are presented in the top two panels of Figure 1. The dominant seasonal feature observed at Alice Springs (23 S) is the semiannual oscillation, as might be expected for a low latitude site. The magnitude of the semiannual OH temperature oscillation is about 4 K, with peak temperatures observed near the equinoxes. At Adelaide (34 S), the higher-latitude site, OH temperatures are governed by an annual oscillation. The amplitude of the annual oscillation at Adelaide is approximately 10 K (20 K peak-to-peak), and peak temperatures are observed near the winter solstice (June/July). The presence of a strong annual signature at Adelaide, and its absence at Alice Springs, is consistent with the predicted latitudinal behavior of the semiannual and annual oscillations, as described above. Both sites also show a long-term downward trend in OH temperatures, which is also observed in the TIMED/SABER data. Part of this apparent cooling trend may be due to the enhanced temperatures observed in 2002 associated with the strong stratospheric warming event observed in the Southern Hemisphere in 2002. Although the data set discussed here is not appropriate for the study of long-term trends, mesospheric changes related to the 2002 stratospheric warming are discussed in a later section.

O2A emission temperature measurements at Alice Springs and Adelaide are presented in the lower two panels of Figure 1. Recall that O2A emissions originate from altitudes above the OH layer; the O2A emission peak is near 94 km, while the OH emissions originate near 87 km [*McDade,* 1998]. In contrast to the lower-altitude OH emission temperatures, there is little latitudinal variation of the O2A temperatures between sites. The semiannual oscillation dominates at both sites, with amplitudes of about 5 K and

temperature maxima near the equinoxes. At Adelaide, the amplitude of the O2A semiannual temperature oscillation appears to be slightly larger than that observed at Alice Springs, and is superimposed upon a general downward temperature trend similar to that observed in the OH temperature data.

OH and O2A emission intensity measurements at Alice Springs and Adelaide are presented in Figure 2. OH emission intensity data show characteristics similar to those of the temperature data presented in Figure 1, showing a dominant semiannual oscillation at Alice Springs and a strong annual variation at Adelaide. O2A emission intensities exhibit a semiannual oscillation at both sites, as was observed in O2A temperatures. However, intensity data exhibit seasonal asymmetries not observed in the temperature data, particularly at Adelaide. For example, OH intensity peaks in May at Adelaide, about one month prior to the observed OH temperature maximum, yet both OH temperature and intensity minima occur nearly simultaneously in January. Equinoctial asymmetry is also evident in the Adelaide O2A intensity data, which shows a large April (autumn) maximum followed by a lesser September (spring) maximum.

3.1 Harmonic analysis of OH and O2A emissions

Harmonic analysis has been frequently used to study the latitudinal behavior of the annual and semiannual oscillations. In analysis presented here, the magnitude and phase of the annual and semiannual oscillations at Alice Springs and Adelaide have been determined by least-squares fit to the data, using the function:

$$F(X) = A_0 + A_1 \cos[2\pi(t - f_1)/365] + A_2 \cos[2\pi(t - f_2)/182.5]$$

where *t* is the day-of-year. Linear trends were removed from the multi-year observations prior to fitting, and data sorted by day-of-year into a single year period. Nightly averages were calculated for each day-of-year using data from a 7-hour period centered on local midnight.

Calculated amplitudes (A_0, $A1$, A_2) and phases (f_1, f_2) of the annual and semiannual components of the OH and O2A emission temperatures and intensities are presented in Tables 1 and 2. TIME-GCM results for each site during the period 2002-2005 were analyzed in a similar manner, with results are presented in italics in the tables below. For comparison, data from comparable sites are also included in the tables. These data are used to highlight the dominant seasonal features as a function of latitude and point out possible site-to-site variations.

Alice Springs (23 S)

Amplitudes and phases of the annual and semiannual oscillations of the mean nightly data at Alice Springs are presented in Table 1. These data are compared to the TIME-GCM results, presented in italics in Table 1. Also shown in Table 1 are data from two sets of ground-based measurements made at Cachoeira Paulista (23 S, 45 W) in 1983-1986 and 1987-1991, and satellite data from UARS/WINDII [*Clemesha et al.,* 1990; *Takahashi et al.,* 1995; *Shepherd et al.,* 2004].

The analysis shows that the dominant semiannual oscillation of OH emission temperatures at Alice Springs has an amplitude of 3.9 K and phase of 84 days, implying

peak temperatures occur near the equinoxes. This dominant semiannual oscillation is also present in the TIME-GCM data, shown in italics in Table 1, although the model tends to overestimate the amplitude of the semiannual oscillation (5.5 K). Both data and model suggest only a weak annual oscillation in OH temperature at Alice Springs; the phase of this annual oscillation is difficult to resolve due to its low amplitude.

The magnitude and phase of the semiannual oscillation observed at Alice Springs is consistent with ground-based measurements made at other low-latitude sites [*Wiens and Weill*, 1973; *Fukuyama*, 1977; *Taylor et al.*, 2005]. A specific example from two observations periods at Cachoeira Paulista (C.P.), located near the western coast of Brazil near the Mantiqueira Mountains, is shown in Table 1. The amplitude of the semiannual component at C.P. is quite similar to that observed at Alice Springs, between 3.0-3.5 K, but the peak OH temperature occurs several weeks later. This phase difference may be due to longitudinal or orographical differences between C.P. and Alice Springs. It may also be an artifact of the analysis, if differing time periods were considered in the nightly averaging at each site. The earlier measurements at C.P. (noted by superscript "a") also show a fairly significant annual oscillation, absent in the other measurements, with a phase suggesting that the April (autumn) temperature maximum is larger than the September maximum.

UARS/WINDII satellite data presented in Table 1 show a much stronger annual oscillation and weaker semiannual oscillation than that observed at Alice Springs or C.P. However, comparisons between satellite and ground-based airglow measurements can be

problematic, since the degree of tidal aliasing varies with observation period. Airglow measurements are limited to a single site but can make continuous nighttime measurements, while satellites make measurements over a wide range of longitudes and local times. The larger annual amplitude and weaker semiannual amplitude measured by satellite could therefore be due to longitudinal averaging, coarser latitudinal resolution, or the tidal aliasing due to differences in local time coverage [*Shepherd et al.,* 2006].

O2A emission temperature analysis results for Alice Springs, presented in Table 1, show a dominant semiannual oscillation, with peak temperatures observed several weeks after the equinoxes. The amplitude of this semiannual oscillation is accurately reproduced by TIME-GCM, although the temperature maximum occurs slightly earlier in the year in the model. Data from TIME-GCM and C.P. also show a significant annual oscillation that is absent from the Alice Springs data. The phase of the annual oscillation in the TIME-GCM O2A temperature data indicates that winter temperatures should be colder than in summer. In contrast, the phase of the larger annual oscillation at C.P. (1983-1986) suggests temperature maxima shifted earlier in the year, but with summer temperatures colder than in winter. The significant phase differences between sites suggest that longitudinal, orographic or wave-induced effects may play a greater role at C.P. that at Alice Springs, especially at higher altitudes. Discrepancies between the observations and the model are difficult to resolve with the analysis presented here, and will be discussed further in the following section with detailed temporal analysis.

Annual and semiannual amplitudes and phases of the OH and O2A emission intensities at Alice Springs are shown in the lower portion of Table 1. Alice Springs OH intensity analysis shows strong annual and semiannual components, with a strong reduction in OH emission intensity observed in summertime (December/January). OH intensity maxima occur about one month later than the OH temperature maxima discussed above. TIME-GCM results predict a weaker annual oscillation than that noted in the observations. The phase of the TIME-GCM annual oscillation suggests a seasonal asymmetry in the equinoctial intensity maxima, with a weak April maximum and strong September maximum. In contrast, observed O2A emission intensities exhibit a very strong semiannual oscillation at Alice Springs, with a weak minimum in wintertime. The TIME-GCM does not reproduce all of the observed amplitudes and phases, and predicts a summertime O2A intensity minimum. The above amplitude differences noted between the data and model may in part be due to the scaling required for comparisons between the model and the data, since model results are sensitive to the emission cross sections used in the model. Sources of phase differences between the data and model are difficult to determine from the analysis presented here, and require more detailed analysis with better temporal resolution.

Adelaide (34 S)

Amplitudes and phases of the annual and semiannual oscillations at Adelaide are presented in Table 2. As was evident in the overview data shown in Figure 1, OH temperatures at Adelaide are dominated by an annual oscillation. The annual component has an amplitude 10.2 K and maximizes shortly after the winter solstice (July). A weaker

semiannual component is also observed, with amplitude of 2.2 K and 22 day phase, effectively steepening the temperature gradients on either side of the solstice. TIME-GCM results at Adelaide predict a slightly weaker annual oscillation and a comparable semiannual oscillation with phase near 94 days. The effect of this semiannual oscillation is to broaden the wintertime temperature maximum, rather than narrow it as observations would suggest.

For comparison, OH temperature data from the Adelaide FTIR spectrometer, spectral airglow temperature data at Sierra Nevada, Spain (37 N), and UARS/WINDII temperatures at 87 km are also shown in Table 2 [*Lopez-Gonzalez et al.*, 2004; *Reid and Woithe*, 2007; *I. Reid, pers. comm.*, 2007; *Shepherd et al.*, 2004]. The FTIR spectrometer data were taken at the same location in Adelaide from September 2001 through February 2006, approximately one year longer than the Aerospace imager data set for that site. A 90 degree phase shift has been added to the FTIR data in Table 2, as the FTIR harmonic fits were done using sine, rather than cosine, functions. The FTIR temperatures show a slightly smaller annual oscillation than that calculated for the imager data and a comparable semiannual oscillation. The effect of this weak semiannual oscillation is to broaden the wintertime temperature maximum, similar to the behavior predicted by the TIME-GCM. Also presented in Table 2 are data from Sierra Nevada (S.N.), a slightly higher-latitude site in the Northern Hemisphere. S.N. observations show a strong annual OH temperature oscillation, peaking near the winter solstice (December/January at this northern site). The semiannual variation of OH temperature is also larger at S.N., effectively broadening the wintertime temperature maximum. The broad wintertime OH

temperature maximum present in the TIME-GCM, FTIR and S.N. data is not evident in the Aerospace imager data, although this apparent discrepancy might be due to differences in the length of the nightly observations periods considered in the analysis. The relationship between the nightly observation period and the extent of the wintertime OH temperature maximum will be further explored in the following section, where detailed analyses of both the temporal and seasonal characteristics are presented.

In contrast to the ground-based measurements, UARS/WINDII satellite measurements at 35 S show a significantly weaker annual temperature oscillation, with peak temperatures observed in May of each year. As was the case at Alice Springs, UARS/WINDII measurements tend to underestimate the dominant oscillation at each site. Discrepancies between the satellite observations may be related to the longitudinal averaging often used in satellite data analysis, as some longitudinal differences have been noted in the ground-based data presented here. Continued comparisons between satellite and ground-based measurements are required to resolve these discrepancies, but are beyond the scope of the analysis presented here.

O2A emission temperature analysis is also presented in Table 2, showing both annual and semiannual components. The weak annual oscillation in O2A emission temperature serves to increase the magnitude of the springtime (September) maximum at Adelaide. The stronger springtime maximum is also observed in the TIME-GCM data, although the semiannual oscillation is somewhat weaker in the model. The TIME-GCM therefore does not reproduce the deep wintertime temperature minimum evident in the data. O2A

temperatures observed at Sierra Nevada and by the Adelaide FTIR spectrometer are also presented in Table 2 [*Lopez-Gonzalez et al.,* 2004; *Reid and Woithe*; 2007]. Sierra Nevada data show a larger annual component than that observed at Adelaide, but the magnitude and phase of the semiannual oscillation is consistent with the observations and the TIME-GCM model. However, O2A temperature data from Reid and Woithe (2007) presented in Table 2 suggest a weaker annual oscillation at Adelaide, accompanied by a significantly larger semiannual oscillation. The combined amplitudes indicate a slightly larger April temperature maximum, in contrast to the stronger September maximum suggested by the imager data. Unfortunately, the discrepancy between the FTIR and imager O2A temperatures is not easily resolved in the temporal analysis described in the following section.

Interestingly, the average O2A temperature measured by the Adelaide spectrometers is 12 K higher than that measured by the Aerospace imager at that site. Recall that Adelaide O2A temperatures were we lowered by about 10 K based on TIMED/SABER calibrations. This absolute temperature discrepancy would suggest that the calculated SABER O2A temperatures might be somewhat high. However, we retain the TIMED/SABER calibration for better site-to-site comparisons.

Amplitude and phases of the annual and semiannual oscillations of OH and O2A emission intensities at Adelaide is presented in the lower portion of Table 2. Harmonic fits to the Adelaide intensity data are complicated by asymmetries in the intensity data present in the overview data (Figure 2). These asymmetries also interfere with fitting of

the TIME-GCM data, resulting in widely disparate amplitudes and phases. The simple harmonic analysis presented here is often not able to fully characterize seasonal features of the data. Inconsistencies between data sets are therefore better illustrated using the combined temporal and seasonal analysis presented in the following section.

3.2 Interannual variability of airglow temperature and intensity

The harmonic analysis presented above is a useful tool for studying seasonal features on a global scale, including site-to-site and data-model comparisons. However, it does not provide useful information about the interannual variability of these seasonal features, nor does it allow investigation of tidal effects or the influence of short-period gravity waves. Results of the harmonic analysis are also quite sensitive to differences in data averaging and the observation period considered. The magnitude of tidal aliasing, for example, can depend on the range of local times considered in the analysis.

A better representation for the interannual variation of airglow temperature and intensity can be found by analyzing data as a function of local time as well as season. In the analysis presented here, imager and TIME-GCM data are binned into 1-hour, 30-day windows. The smoothing provided by the 30-day bins effectively removes gaps due to moon-up and cloudy periods, allowing easier identification of seasonal features. However, the seasonal features described here can be observed even at higher resolution (up to 10 day binning). Nighttime observations by the ground-based imagers limit useable data to an 8-hour window centered about local midnight, 14:30 UT, at both observation sites. Note that this 8-hour window does not allow for definitive determination of diurnal or semidiurnal tides, although the existence of a semidiurnal tide

can be inferred in some cases. It is possible to distinguish the terdiurnal tide in the daily 8-hour data; however, it does not often dominate the monthly averages plotted here.

Results of the seasonal-temporal data analysis are presented in Figures 3-18. A guide for the reader is offered in Tables 3 and 4, where the significant seasonal features of the data are summarized. Occurrence times of equinoctial and solstice minima and maxima are noted in the tables, and agreement with the TIME-GCM is noted by typeset: features that are accurately reproduced in the TIME-GCM model are given in bold type; those absent from the model are shown in plain type. Unexplained phase shifts or improper time-localization in the model is indicated by italics, and discrepancies between measured and observed intensities, particularly as compared to other maxima/minima, are designated by underlined text.

3.2.1 OH emission temperature and intensity

Alice Springs (23 S)

OH emission temperatures measured at Alice Springs binned in one-hour and one-month increments are presented in Figure 3. OH emission temperature data from the TIME-GCM at Alice Springs are shown for comparison in Figure 4. Both data and model show that the equinoctial temperature maxima associated with the semiannual oscillation occur primarily in the morning hours, near 18 UT. While the equinoctial temperature maxima are well-represented by the TIME-GCM, the temporal variation of the solstice minimum temperature is not. Summertime (January) OH temperature minima are observed in the early evening hours (11 UT) and are generally colder than winter temperatures. Winter minima occur several hours, at about 16 UT. The TIME-GCM does not reproduce the

observed temporal variation of the solstice minima, instead predicting nearly continuous solstice minima over the course of the night. The model also tends to overestimate the magnitude of the wintertime minimum. Recall that the harmonic analysis, above, indicated that the TIME-GCM overestimated the magnitude of the semiannual oscillation at Alice Springs. The analysis presented in Figures 3 and 4 suggest that the source of the model overestimation the difference between the observed and predicted period of observed low temperatures at the summer and winter solstices.

Although the seasonally phase shifted pattern of solstice temperature minima (evening-winter/midnight-summer) is observed throughout the four-year observation period, the solstice temperatures are noticeably warmer in 2002. Observed equinoctial temperature maxima are also warmer in October 2002 and March 2003. This overall warming trend in the second half of 2002 is associated with the strong stratospheric warming event observed in the Southern Hemisphere in September 2002 [see *J. Atmos. Sci., special issue*, 2005; *Dowdy et al.*, 2004]. The observed warming period extends from June 2002 through March 2003, which is consistent with other 2002 stratospheric warming observations, but longer than that predicted by the TIME-GCM.

OH emission intensity data for Alice Springs are presented in Figure 5; corresponding TIME-GCM data are shown in Figure 6. Equinoctial maxima are observed in the early evening hours (11 UT) in both the data and the model. The observations also show a second equinoctial maxima in October of each year, which roughly corresponds to a weak equinoctial maxima predicted by the model. However, the TIME-GCM predicts

morning equinoctial maxima in both April and October, with the October maximum occurring slightly earlier in the night. The comparison between the data and the model suggests that the predicted seasonal asymmetry in the timing of the morning equinoctial maxima is also present in the Alice Springs OH intensity data, but that the morning maxima occur slightly later in the evening than predicted by the model.

Careful examination of the Alice Springs OH intensity data in Figure 5 also show seasonally-varying pattern of solstice OH intensity minima with phase shifts similar to that observed in the OH temperature data described above. However, observed OH intensity minima occur later in the evening than the corresponding OH temperature minima: summertime intensity minima are observed near midnight (14:30 UT) and wintertime intensity minima in the morning (18 UT). The observed OH intensity minima are particularly strong in 2004, the same year in which OH temperatures exhibited deep minima at both solstices (Figure 3). The TIME-GCM reproduces the general structure of the observed OH intensity minima, but does not accurately represent of the magnitudes of the summertime and wintertime minima. The discrepancy between the data and the model is particularly noticeable in January 2004, where the model fails to replicate the deep OH intensity minima measured by the imager. Note also that the TIME-GCM predicts large excursions of OH intensity associate with the 2002 stratospheric warming in late 2002 that are not observed in the Alice Springs OH intensity data. Curiously, although the 2002 stratospheric warming resulted in significant changes in OH temperature structure shown in Figure 3, no corresponding effects were observed in the OH intensity data (Figure 5).

Adelaide (34S)

Adelaide OH emission temperature data is presented as a function of local time and season in Figure 7, with corresponding TIME-GCM model data presented in Figure 8. The dominant annual oscillation at Adelaide is characterized by a strong summertime temperature minimum in the evening (11 UT), and double-peaked temperature maxima in morning in wintertime. Recall that Adelaide FTIR harmonic analysis, above, suggested a broadened or double-peaked wintertime maximum. The data presented in Figure 7 suggests that slight differences in the observation window used in the harmonic analysis likely accounts for the differences between the Adelaide FTIR and imager data noted in Table 2. The OH temperatures observed by the imager appear to be slightly warmer in September than in May, which is opposite that predicted by TIME-GCM. The model also does not accurately reproduce the local-time dependence or the depth of the observed summertime temperature minimum, and predicts a weak winter OH temperature minimum that is not observed. However, the model does accurately represent the temperature enhancements associated with the 2002 stratospheric warming period at Adelaide. Note that effect of the stratospheric warming on OH temperature measurements appears to be slightly weaker at Adelaide than at Alice Springs.

OH emission intensities observed at Adelaide and produced by the TIME-GCM are presented in Figures 9 and 10, respectively. A deep OH intensity minimum is observed in late summer (February/March), reflecting the dominant annual oscillation at Adelaide. Note that this OH intensity minimum occurs approximately one month later than the

corresponding OH temperature minimum shown in Figure 7. This month-long delay in the observation of the OH intensity minimum is not evident in the model, which predicts a January minimum, and is likely responsible for the discrepancies between data and model noted in the harmonic analysis, above. TIME-GCM also predicts weaker July OH intensity minima, signs of which occur occasionally in the data.

Quasi-equinoctial OH intensity maxima are present in both observations and model data at Adelaide, peaking in May and August. However, TIME-GCM predicts that equinoctial maxima in the evening hours, near 11 UT, while the observations show intensity enhancements in both the morning and evening. Morning (18 UT) intensity maxima follow the predicted May/August quasi-equinoctial pattern, while evening (11 UT) maxima are less well-organized. Strong evening maxima often occur in July, a seasonal signature completely absent from the model. Note that the July evening maximum is occasionally present at Alice Springs, as well (Figure 5), although it was observed to be much smaller than the equinoctials maxima at that site. There is some evidence that the July maximum is due to higher-order (semidiurnal or terdiurnal) tides, since the 11 UT intensity maximum is occasionally accompanied by a morning maximum (at Adelaide) or minimum (at Alice Springs). Overall, the Adelaide OH intensity observations presented here show very little agreement with the TIME-GCM model.

3.2.2 O2A emission temperature and intensity

Alice Springs (23 S)

O2A temperature data from Alice Springs are presented in Figure 11; corresponding TIME-GCM data is shown in Figure 12. The temperature structure of the O2A emissions

at Alice Springs is very similar to that of the OH emissions at site. Equinoctial maxima occur in the morning hours (18 UT), summer solstice minima are observed at 11 UT, and winter solstice minima at 16 UT. However, wintertime O2A temperatures are colder than summertime temperatures, although the reverse was observed in the OH data presented in Figure 3. The TIME-GCM model reproduces the colder winter O2A temperatures observed at Alice Springs, but again fails to reproduce the temporal localization of the winter solstice minima. Equinoctial O2A temperature maxima are observed in the early morning hours at Alice Springs, and are generally well-represented in the TIME-GCM. However, the model predicts an enhancement of the October maximum not evident in the data. In contrast to the Alice Springs OH emission temperature data presented in Figure 3, the O2A temperatures shown here do not respond significantly to the stratospheric warming event in late 2002, but do show some enhancement in March 2003.

Alice Springs O2A intensity data, presented in Figure 13, closely mimic the O2A temperature data of Figure 11, with an identical seasonal phase shift in emission intensity at the solstices. Unlike the OH emission data presented earlier, O2A intensity minima occur simultaneously with O2A temperature minima. The TIME-GCM O2A emission data, presented in Figure 14, accurately reproduces this one-to-one temperature/intensity relationship, although the O2A temperatures determined by the model are not accurate (Figure 12). In contrast to the O2A temperature data, O2A intensities at Alice Springs increase significantly in October 2002 and March 2003 during the stratospheric warming event. The TIME-GCM predicts a slight intensity enhancement in October 2002, but generally does not reproduce the 2002 O2A intensity observations at Alice Springs.

Adelaide (34 S)

O2A temperatures measured at Adelaide are shown in Figure 15. As was the case at Alice Springs, O2A temperatures at Adelaide exhibit seasonal and temporal behavior similar to that observed in the OH emissions at that site. Strong temperature maxima are observed in the morning hours at the equinoxes and deep minima in the evening at the summer solstice. However, the secondary wintertime temperature minimum is stronger here than in the OH temperature data for this site; the TIME-GCM again overestimates the depth of this winter temperature minimum (Figure 16). O2A temperatures are significantly warmer in 2002, with temperatures enhancements comparable to those predicted by TIME-GCM.

Adelaide O2A emission intensity data are presented in Figure 17 and corresponding TIME-GCM data shown in Figure 18. Adelaide O2A intensities show a general increase in strength over the course of the night, particularly near the equinoxes, but do not exhibit well-defined structure near the solstices. A strong April maximum is observed in the morning hours in 2002, 2003, and 2004, but the TIME-GCM predicts stronger October maxima. There is a rough correlation between the O2A temperature and intensity data, but the agreement is not as clear as it was at Alice Springs. The TIME-GCM data struggles to mimic the somewhat disorganized seasonal structure of the Adelaide O2A emission data.

4 Discussion

The data presented here demonstrate the temporal and seasonal variations of OH and O2A emissions at two Australian sites. The dominant features observed at the equinoxes, solstices, and during the 2002 stratospheric warming event are summarized in Tables 3 and 4. The TIME-GCM successfully reproduces many of the temporal and seasonal characteristics of the observations, including the equinoctial behavior and stratospheric warming response. Disagreements between the data and model occur primarily near the solstices, where seasonal phase shifts and winter/summer temperature ratios are frequently misrepresented by the model. In the following discussion, we first consider temperature and intensity maxima observed at both sites. These maxima are frequently observed near the equinoxes, but share some characteristics with intensity maxima occasionally observed near the solstices. We then discuss temperature and intensity minima, as these appear to share some common characteristics between sites.

4.1 Temperature and Intensity Maxima

Alice Springs equinoctial maxima

The semiannual oscillation is clearly dominant at Alice Springs, where strong temperature and intensity maxima are observed near the equinoxes. These equinoctial maxima are prominent for only part of the night; OH emission temperatures maximize at the equinoxes in the morning hours (18 UT), while OH intensities are higher in the evening (12 UT), and both O2A temperatures and intensities peak in the morning hours. The 6-hour phase difference between the OH intensity and temperature maxima is consistent with the predicted Krassovsky phase for the migrating diurnal tide, which is

the likely source for semiannual oscillations at low latitudes [*Walterscheid and Schubert,* 1995].

Since the TIME-GCM appears to reproduce most features of the Alice Springs equinoctial observations, it becomes a useful tool for highlighting weaker features in the data that might have gone unnoticed. In addition to the 6-hour phase difference between OH temperature and intensity maxima described above, the model also predicts a 2-hour phase difference between O2A temperatures and intensities. This feature is not obvious from a cursory review of the data presented here, but when compared to the TIME-GCM model, it appears that O2A temperatures maximize slightly earlier in the night than the corresponding O2A emission intensities. Definitive confirmation of this 2-hour phase shift is difficult over the limited observation period available here, but may be possible with larger data sets. Analysis of these smaller phase shifts may lead to improvements in seasonal-tidal coupling in the model.

The model results also provide an explanation for the strong October OH intensity maximum observed in the morning hours at Alice Springs. The TIME-GCM predicts weak morning equinoctial maxima, in addition to the evening maxima, with a seasonal phase shift such that the April maximum occurs later in the evening than the October maximum. The seasonal phase shift predicted by the model is observed in the data as a single springtime (October) maximum, indicating that the onset of the April maximum occurs outside of the nightly observation window. The model predicts similar seasonal phase shifts for both emissions at Alice Springs, although the data do not indicate that it

is a dominant feature in other than the OH intensity data. A seasonal phase shift is indicated in the OH and O2A temperature data in 2004, but appears to be obscured by significant temperature variations in other years.

The seasonal phase shift predicted by the model observed is also consistent with springtime enhancements observed at other tropical sites, for example, the springtime increase in OH and O2A temperatures and intensities observed at Maui [*Taylor et al.*, 2005]. However, the existence of strong springtime maxima in both emissions at Maui, as opposed to primarily in OH intensity at Alice Springs, may indicate differences in day-to-day temperature and intensity variability between sites. Further investigation is needed to determine how daily variations obscure the underlying tidal signatures predicted by the model.

Adelaide equinoctial maxima

At Adelaide, equinoctial temperature and intensity maxima appear slightly shifted toward the winter solstice, occurring in May and September. These quasi-equinoctial maxima occur primarily in the morning hours, with secondary OH intensity enhancements present in the evening hours. The TIME-GCM accurately reproduces most of the Adelaide observations, including the winter-ward shift of the equinoctial maxima.

However, the TIME-GCM prediction for the seasonal OH intensity structure at Adelaide differs significantly from the observations. The model indicates that equinoctial OH intensity maxima should occur only in the early evening hours, as was predicted and

observed at Alice Springs. However, the Adelaide data show strongest equinoctial maxima in the morning hours, accompanied by only weak maxima in the evening. If evening maxima are associated with the diurnal tide, as was the case at Alice Springs, then suppression of the evening maxima might be expected to occur at higher latitudes, where the strength of the diurnal tide is greatly diminished.

The existence of strong morning OH intensity maxima at Adelaide is puzzling, but may be related to a change in the mesospheric temperature profile over the course of the night. The OH intensity maxima appear fairly well correlated to the OH temperature maxima, at least in alternate years (2002 and 2004). Lidar measurements at Starfire Optical Range, NM show an overall downward phase propagation of the mesopause in April and October [*Chu et al*., 2005]. The downward phase progression means warm air is found at lower altitudes, resulting in an increase in temperature from 85-90 km in the morning hours. This downward phase propagation essentially pumps atomic oxygen downward, leading to an increase in the OH intensity coincident with observed pre-dawn warming.

Solstice maxima

In addition to the morning intensity maxima, evening maxima of OH intensity are observed at the winter solstice (July), and are also absent from the model. These winter solstice maxima are also observed at Alice Springs, and again are absent from the TIME-GCM data for that site. Curiously, evening winter solstice minima are predicted in TIME-GCM data prepared for the WINDII/UARS comparison, albeit at latitudes poleward of 40 degrees in the Southern Hemisphere [*Shepherd et al.*, 2005]. Wintertime

lidar temperature data taken at Maui and Starfire Optical Range show a cold region at higher altitude that disappears quickly in the early evening, perhaps providing a source of atomic oxygen at lower altitudes for the observed OH intensity enhancement [*Chu et al.*, 2005]. However, there is no indication of an enhancement of O2A intensity at the winter solstice at either Alice Springs or Adelaide. Further examination of the model is therefore needed in order to determine the origin of this winter solstice feature.

4.2 Temperature and Intensity Minima

Alice Springs solstice minima

Minima in OH and O2A temperature and intensity occur at both the summer and winter solstice at Alice Springs. Summertime (December/January) OH temperatures are coldest in the early evening, followed by gradual warming after midnight. In contrast, the wintertime (July) OH temperature minimum occurs after midnight, and is warmer than the summertime minimum by 10-15 degrees. O2A temperatures at Alice Spring follow a similar seasonal pattern: evening summertime minima, and morning wintertime minima. However, wintertime O2A temperatures are colder than summertime O2A temperatures at Alice Springs. A comparison between the observed temperature minima at each solstice show that while OH temperatures are colder than O2A temperatures in summer, the reverse is true in winter. This seasonal change in the altitude of the cold-temperature region is consistent with a higher altitude mesopause in winter [*She and von Zahn*, 1998]. Although altitude differences between the summer and winter mesopause have been established, the origin of the temporal phase shift between summer and winter maxima as observed here is still unclear. This temporal phase shift in the observed solstice

temperature minima at Alice Springs is not reproduced by the TIME-GCM, which also tends to overestimate the depth of the wintertime OH temperature minimum.

OH intensity minima observed at Alice Springs exhibit a temporal phase shift similar to that seen in the OH temperature data, with summertime minima occurring earlier in the night than wintertime minima. However, OH intensity minima are shifted forward in time by about 4 hours with respect to the corresponding temperature minima. This 4-hour phase shift between OH temperature and intensity is shorter than expected for the diurnal tide [*Walterscheid and Schubert*, 1995]. This 4-hour phase shift between summertime and wintertime OH temperature minima is not reflected in the TIME-GCM data, in part because of the lack of temporal localization of the temperature minima noted above.

Since the diurnal tide is weakest near the solstices, it is possible that other wave phenomena are responsible for the emission and intensity phase shifts near the solstices. Seasonal phase shifts have been observed in MF radar wind data at Kauai, HI (22 N), and are assumed to be associated with interfering wave modes, including non-migrating tides and gravity waves [*Vincent et al.*, 1998]. Diurnal tides are weakest near the solstices, and weak tides may be subject to significant damping by gravity waves [*Roble and Shepherd*, 1997]. The inability of the model to reproduce the observed solstice behavior may, therefore, be due to an inaccurate gravity wave representation in the model, since the TIME-GCM does not include seasonal variation of gravity waves.

We first consider the correlation between OH emission intensity and gravity wave flux at Alice Springs. OH intensity can respond to changes in the vertical diffusion constant, K_{zz}, as higher K_{zz} leads to lower atomic oxygen densities and reduced OH emission [*LeTexier et al.,* 1987]. K_{zz} maximizes in summer in the mesosphere, with a secondary maximum at lower altitudes (75 km) in wintertime, and is influenced by gravity wave breaking. Gravity wave activity can be determined from the imager data by calculating the percentage of nights in which the variation of intensity across the image exceeds a designated threshold. This measurement serves as a proxy for strong gravity wave activity, given for Alice Springs and Adelaide in Figures 19 and 20, shown in arbitrary units.

Examination of OH intensity data at Alice Spring illustrates a close connection between gravity waves and seasonal changes in the airglow emissions. Strong OH intensity minima are observed near midnight in February/March of each year. However, the magnitude of this summertime OH intensity minimum is not uniform from year-to-year, and appears highly correlated with gravity wave occurrence frequency. Gravity wave fluxes in early 2004 are significantly weaker than in other years, and this minimum in gravity wave flux matches a deep minimum in OH emission intensity observed in summer 2004. This suggests that the summertime OH intensity minima, and likely the corresponding temperature minima, are largely determined by gravity wave dynamics, rather than the diurnal tide. While summertime temperature and intensity minima might be explained by seasonal variations in the gravity wave flux, wintertime solstice behavior does not appear to be correlated to the wave fluxes shown in Figure 19. Differences in

the gravity wave spectra in wintertime or interactions between weak waves and the weak diurnal tide may play a role in the dynamics that control the wintertime mesosphere. Seasonal differences in gravity wave propagation have been observed at Adelaide, which may result in a phase shift when coupled with the diurnal tide [*Reid and Woithe*, 2005]. Further investigation requires detailed determination of gravity wave spectra at both Australian sites, which is currently in progress.

Adelaide solstice minima

At Adelaide, strong OH temperature and intensity minima occur primarily in summertime, with coldest temperatures observed in the evening hours. This is similar to the summertime temperature structure observed at Alice Springs, which was attributed to strong gravity wave fluxes near the summer solstice. As was the case at Alice Springs, a 4-hour delay between the local-time occurrence of the OH temperature minima and corresponding OH intensity minima is observed. The evening-localization of the OH temperature minima and the time delay between summertime OH temperature and intensity minima are again absent in the TIME-GCM results.

O2A temperatures and intensities at Adelaide also have strong summertime minima, but are also accompanied by a weak wintertime minima. Summertime OH temperatures are colder than O2A temperatures; the reverse is true in wintertime, although wintertime temperatures are still significantly warmer than summertime temperatures. This is consistent with an overall increase in the altitude of the mesopause in winter, perhaps to higher altitudes than at Alice Springs, and possibly accompanied by some weakening.

Although the TIME-GCM correctly predicts low summertime OH temperatures, it fails to show the post-midnight warming in of the OH layer, and also overestimates the magnitude of the wintertime O2A temperatures.

Once again, there is good inverse correlation between gravity wave fluxes (Figure 20) and OH intensity minima at Adelaide. However, while a strong seasonal phase shift is observed between summer and winter OH intensity minima at Alice Springs, no significant phase shift is observed at Adelaide. The absence of any summer/winter phase shift is confirmed by the O2A intensity data at Adelaide, which show deep intensity minima at midnight in both winter and summer. The lack of any significant diurnal tide at this mid-latitude site removes a significant source of wave-wave interaction, and may explain the absence of any seasonal phase shift at Adelaide.

4.3 2002 Stratospheric warming

A major stratospheric warming event occurred in the Southern Hemisphere in September 2002 [see *J. Atmos. Sci., special issue,* 2005]. Although minor warming events have been observed in the Southern Hemisphere, this was the first recorded major warming event in the Southern Hemisphere, and was associated with a breakdown of the polar vortex [*Hernandez et al.,* 2003; *Kruger et al.,* 2004]. Signs of anomalous warming were observed as early as May 2002 [*Harnik et al.,* 2005]. In June 2002, planetary waves associated with preconditioning of the atmosphere prior to significant warming were observed at three high-latitude radar sites, Davis, Syowa, and Rothera [*Dowdy et al.,* 2004]. Stratospheric warming generally results in mesospheric cooling at high latitudes [*Cho et al.,* 2004; *Walterscheid et al.,* 2002]. Changes in global circulation associated

with the stratospheric warming at high latitudes can result in stratospheric cooling, and associated mesospheric warming at low latitudes.

Enhancements in emission temperature associated with the 2002 stratospheric warming were observed at both Australian sites, as summarized in Tables 3 and 4. The period of observed warming began in early 2002 and, at Alice Springs, extended into early 2003. Warming effects were significant in both OH and O2A temperatures at Adelaide, but were largely confined to OH temperatures at Alice Springs. Many features of the warming were present in the TIME-GCM data, although the model in all cases predicted a significantly shorter period of enhanced temperatures.

Although weak stratospheric warming effects were observed in O2A intensities at both sites, neither site showed any warming effects in OH emissions. The TIME-GCM predicted intensity enhancements in O2A emissions at both sites, and significant changes in OH emission intensities were predicted at Alice Springs throughout 2002. The lack of any change in OH intensity at Alice Springs, in spite of the strong stratospheric warming effects predicted by the model, is intriguing. Closer examination of this time period in both the data and the model, including characterizations of planetary waves at each site, will be the subject of future work.

5 Summary

The data presented here have been used to explore the interannual variations of OH and O2A emissions at two proximate sites, Alice Springs and Adelaide, over a 4-year period. The site-to-site and data-model comparisons discussed here are meant to show the extent

of interannual variability in the observations and suggest possible avenues for further investigation. It was found that the TIME-GCM successfully reproduces many features observed in the data, particularly the equinoctial signatures associated with the diurnal tide. Several discrepancies noted between the observations and the model may be attributed to an inadequate model specification of the seasonal variation of gravity waves, which were shown above to be correlated with the strength of solstice minima. The model also successfully described many of the changes observed during the 2002 stratospheric warming event.

Significant findings presented in this paper include:

Significant data/model agreement:

- The TIME-GCM reproduces most features of the equinoctial maxima, particularly at the lower latitude site (Alice Springs) where the diurnal tide dominates the dynamics.
- A 6-hour phase shift observed between the equinoctial OH temperature and intensity maxima at Alice Springs is consistent with TIME-GCM predictions. This phase shift is consistent with the Krassovsky phase shift expected for the diurnal tide, and confirms this as the dominant tidal mode at the equinoxes at Alice Springs.
- The October (springtime) enhancement of OH intensity observed at Alice Springs is better explained through comparison with the model, which predicts the occurrence of the springtime (October) maximum earlier in the night relative to

the April maximum. Springtime maxima have been observed at other sites, and are presumably the result of similar tidal phase shifts [*Taylor et al.,* 2005].

- The TIME-GCM successfully predicts temperature enhancements related to the 2002 Southern Hemisphere stratospheric warming event.
- Weak enhancements in O2A intensity observed in September/October 2002 at both sites are well-represented by the TIME-GCM. O2A emissions at Alice Springs also increased in March 2003, not predicted in the TIME-GCM, but appear correlated to Alice Springs OH and O2A temperatures.

Minor data/model agreement:

- The TIME-GCM predicts cooler wintertime O2A temperatures, as compared to wintertime OH temperatures, as observed. However, as discussed in the text, this agreement is somewhat obscured by the tendency of the TIME-GCM to overestimate wintertime OH temperature minima.
- The TIME-GCM reproduces the one-to-one correspondence between O2A temperature and intensity at both sites. However, the model often does not accurately predict the observed O2A temperature structure, leading to discrepancies between the O2A intensity observations and model results.

Significant data/model disagreement:

- TIME-GCM overestimates the depth of the wintertime OH temperature minimum at both sites. The large gravity wave fluxes observed in January at each site are not represented in the model, which uses a seasonally invariant gravity wave

parameterization. Therefore, the model results likely indicate an underestimation of the summertime temperature minima, rather than an overestimation of the wintertime minima. This summertime temperature anomaly also affects O2A temperatures at both sites.

- TIME-GCM does not reproduce the temporal localization of the solstice OH temperature minima at both sites. TIME-GCM OH temperature minima occur at the wrong local time or span too long a time period. It is possible that this improper time localization in the model is due to inadequate specification of the seasonal variation of gravity wave flux at both sites.
- OH intensity maxima are not well-represented by TIME-GCM, which seems to predict a 6-hour phase shift between OH temperatures and intensities similar to that observed at Alice Springs. The lack of phase shift indicates that the diurnal tide is not prevalent at Adelaide, and equinoctial behavior is determined by other processes (semidiurnal, terdiurnal, planetary waves, etc.).
- July evening OH intensity maxima (11 UT) are observed at both sites, but not predicted by TIME-GCM. This curious behavior at the winter solstice may be due to higher-order tides (semidiurnal, terdiurnal) at the winter solstice, where the diurnal tide is expected to be significantly weakened but gravity wave fluxes not as significant; planetary waves may also play a role. These processes will be investigated in future work.
- Alice Springs experienced significant a significant increase in OH temperature over an extended period of time, June 2002- March 2003, with no accompanying

OH intensity increase. An increase in both OH intensity and temperature in late 2002 was predicted by the TIME-GCM.

Minor data/model disagreement:

- A 4-hour time lag is observed between OH temperature minima and OH intensity minima at both sites. The TIME-GCM does not produce this phase shift, in part because of the lack of proper temporal localization of OH temperatures and inaccurate representation of OH intensities at the solstices.
- A May (autumn) enhancement of OH and O2A intensity is observed at Adelaide. This enhancement is not predicted by the TIME-GCM, but is consistent with measurements at other mid-latitude sites and an the annual April/May enhancement in the O(^{1}S) emission observed by WINDII/UARS [*Taylor et al.*, 2001; *Shepherd et al.*, 2006].
- Alice Springs O2A temperatures differ significantly from the model during the 2002 stratospheric warming period.

The imagers operating at Alice Springs and Adelaide have produced a vast amount of data, only a portion of which is presented here. It is clear from the analysis described here that the length of the nightly observation window can significantly affect the calculated annual and semiannual amplitudes if nightly averages are assumed. Apart from the effect on harmonic analysis results, the temporal variation of the seasonal temperature and intensity structure introduced here suggests that interactions of various wave modes affect mesospheric conditions. Planetary wave, higher-order tide and

gravity wave signatures can be extracted from the Australian data set, and continue to be analyzed, with the hope of resolving some of the unexplained features associated with the solstice observations. Continued development of the TIME-GCM and additional measurements at both sites are needed to fully characterize the features described here.

Acknowledgements

This work was supported under The Aerospace Corporation's Independent Research and Development Program and NSF grant ATM-0436516.

References

Andrews, D. G., J. R. Holton, and C. B. Leovy (1987), Middle Atmosphere Dynamics, Academic Press, Inc., Orlando, Florida, pp. 489.

Buriti, R.A.; Takahashi, H.; Gobbi, D.; de Medeiros, A.F.; Nepomuceno, A.A.; Lima, L.M. (2004), Semiannual oscillation of the mesospheric airglow at 7.4°S during the PSMOS observation period of 1998-2001, *J. Atm. Solar-Terr. Phys, 66, (6-9),*567-72.

Cho, Y.-M., G. G. Shepherd, Y.-I. Won, S. Sargoytchev, S. Brown, and B. Solheim (2004), MLT cooling during stratospheric warming events, *Geophys. Res. Lett., 31*, L10104, doi:10.1029/2004GL019552.

Chu, X., C. S. Gardner, and S. J. Franke (2005), Nocturnal thermal structure of the mesosphere and lower thermosphere region at Maui, Hawaii (20.7_N), and Starfire Optical Range, New Mexico (35_N), J. Geophys. Res., 110, D09S03, doi:10.1029/2004JD004891.

Clemesha, B.R., H. Takahashi, P.P Batista (1990), Mesopause temperatures at 23S, *J. Geophys. Res., 95,* 7677-7681.

Dowdy, A. J., R. A. Vincent, D. J. Murphy, M. Tsutsumi, D. M. Riggin, and M. J. Jarvis (2004), The large-scale dynamics of the mesosphere–lower thermosphere during the

Southern Hemisphere stratospheric warming of 2002, *Geophys. Res. Lett.*, *31*, L14102, doi:10.1029/2004GL020282.

Dunkerton, T. J. (1982), Theory of the mesopause semiannual oscillation, *J. Atmos. Sci.*, *39*, 2681-2690.

Forbes, J.F. (1995), Tidal and Planetary Waves, The Upper Mesosphere and Lower Thermosphere: A Review of Experiment and Theory, American Geophysical Union Geophysical Monograph 87, pp. 67-87.

Fritts, D.C. (1995), Gravity wave-tidal interactions in the middle atmosphere: observations and theory, The Upper Mesosphere and Lower Thermosphere: A Review of Experiment and Theory, American Geophysical Union Geophysical Monograph 87, pp. 121-131.

Fukuyama, K. (1976), Airglow variations and dynamics in the lower thermosphere and upper mesosphere--I. Diurnal variation and its seasonal dependency, *J. Atm. Terr. Phys.*, *38*, 1279-1287.

Fukuyama, K. (1977), Airglow variations and dynamics in the lower thermosphere and upper mesosphere--II. Seasonal and long-term variations, *J. Atm. Terr. Phys. 39*, 1-14.

Garcia, R.R., T.J. Dunkerton, R.S. Lieberman, R.A. Vincent (1997), Climatology of the semiannual oscillation of the tropical middle atmosphere, JGR 102, 26019-26032.

Harnik, N. (2005), R.K. Scott, J. Perlwitz, Wave Reflection and Focusing prior to the Major Stratospheric Warming of September 2002, J. Atm. Sci., 62, 640–650.

Hecht, J.H., R.L. Walterscheid, M.N. Ross (1994), First measurements of the two-dimensional horizontal wave number spectrum from CCD images of the nightglow, *J. Geophys. Res., 99* (A6), 11,449-11,460.

Hecht, J.H., R.L. Walterscheid, J. Woithe, L. Campbell, R.A. Vincent, I.M. Reid (1997), Trends of airglow imager observations near Adelaide, Australia, GRL, 24 (5), 587-590.

Hecht, J.H.; Walterscheid, R.L.; Vincent, R.A. (2001), Airglow observations of dynamical (wind shear-induced) instabilities over Adelaide, Australia, associated with atmospheric gravity waves, *J. Geophys. Res.,106 (D22)*, 28189-97.

Hecht, J.H.; Kovalam, S.; May, P.T.; Mills, G.; Vincent, R.A.; Walterscheid, R.L.; Woithe, J. (2004), Airglow imager observations of atmospheric gravity waves at Alice Springs and Adelaide, Australia during the Darwin Area Wave Experiment (DAWEX), *J. Geophys. Res., 109 (D20)*, 10.1029/2004JD004697

Hernandez, G. **(**2003), Climatology of the upper mesosphere temperature above South Pole (90°S): Mesospheric cooling during 2002, *Geophys. Res. Lett., 30*(10), 1535, doi:10.1029/2003GL016887.

Holton, J. R. (1983), The influence of gravity wave-breaking on the general circulation of the middle atmosphere, *J. Atmos. Sci., 40,* 2497-2507.

Krüger, K., B. Naujokat, K. Labitzke, (2005) The Unusual Midwinter Warming in the Southern Hemisphere Stratosphere 2002: A Comparison to Northern Hemisphere Phenomena, *J. Atmos. Sci., 66,* 603-613.

LeTexier, H., S. Solomon, R.R Garcia (1987), Seasonal variability of the OH Meinel bands, *Planet. Space Sci., 35(8),* 977-989.

Lindzen**,** R.S. (1981), Turbulence and stress owing to gravity wave and tidal breakdown, *J. Geophys. Res., 86 (C10),* 9707-14.

Liu, H.-L., Roble, R.G. (2002), A study of a self-generated stratospheric sudden warming and its mesospheric–lower thermospheric impacts using the coupled TIME-GCM/CCM3, *J. Geophys. Res. 107 (D23),* 4695.

Lopez-Gonzalez, M. J., E. Rodrıguez, R. H. Wiens, G. G. Shepherd, S. Sargoytchev, S. Brown, M. G. Shepherd, V. M. Aushev, J. J Lopez-Moreno, R. Rodrigo, Y.-M. Cho (2004), Seasonal variations of O2 atmospheric and OH(6–2) airglow and temperature at mid-latitudes from SATI observations, *Annales Geophysicae*, *22*, 819–828.

Marsh, D. R., A. K. Smith, M. G. Mlynczak, and J. M. Russell III (2006), SABER observations of the OH Meinel airglow variability near the mesopause, *J. Geophys. Res., 111,* A10S05, doi:10.1029/2005JA011451.

McDade, I.C. (1998), The photochemistry of the MLT oxygen airglow emissions and the expected influences of tidal perturbations, *Adv. Space Res., 21 (6),* 787-794.

McLandress, C. (2002), Interannual variation of the diurnal tide in the mesosphere induced by a zonal-mean wind oscillation in the tropics, *Geophys. Res. Lett., 29,* 10.1029/2001GL-14551.

Ortland, D. A., M. J. Alexander (2006), Gravity wave influence on the global structure of the diurnal tide in the mesosphere and lower thermosphere, *J. Geophys. Res., 111,* A10S10, doi:10.1029/2005JA011467.

Reid, I. M., and J. M. Woithe (2005), Three-field photometer observations of short-period gravity wave intrinsic parameters in the 80 to 100 km height region, *J. Geophys. Res., 110,* D21108, doi:10.1029/2004JD005427.

Reid, I.M., J.M. Woithe, The variability of the 558 nm OI airglow intensity measured over Adelaide, Australia, *J. Adv. Space Res.(in press)* (2007), doi:10.1016/j.asr.2007.01.061.

Roble, R.G., E.C. Ridley (1994), A thermosphere-ionosphere-mesosphere-electrodynamics general circulation model (TIME-GCM): Equinox solar cycle minimum simulations (30-500 km). *Geophsy. Res. Lett., 21,* 417-420.

Roble, R.G., G.G. Shepherd (1997), An analysis of wind imaging interferometer observations of O(^{1}S) equatorial emission rates using the thermospheric-ionospheric-mesospheric-electrodynamics general circulation model, *J. Geophys. Res., 102,* 2467-2474.

She, C.Y., U. von Zahn (1998), Concept of a two-level mesopause: Support through new lidar observations, *J. Geophys. Res.*, 103 (D5), 5855-5863.

Shepherd, M. G., W. F. J. Evans, G. Hernandez, D. Offermann, and H. Takahashi (2004), Global variability of mesospheric temperature: Mean temperature field, *J. Geophys. Res., 109, D24117,* doi:10.1029/2004JD005054.

Shepherd, G.G., G. Liu, R.G. Roble (2005), Large-scale circulation of the atomic oxygen in the upper mesosphere and lower thermosphere, *Adv. Space Res., 35,* 1945-1950.

Shepherd, G.G., Y.-M. Cho, G. Liu, M.G. Shepherd (2006), Airglow variability in the context of global mesospheric circulation, JASTP 68, 2000–2011.

Takahashi, H., B.R. Clemesha, P.P. Batista (1995), Predominant semi-annual oscillation of the upper mesospheric airglow intensities and temperatures in the equatorial region, *J. Atm. Terr. Phys., 57,* 407-414.

Taylor, M. J. ; Pendleton, W. R., Jr. ; Liu, H.-L. ; She, C. Y. ; Gardner, L. C. ; Roble, R. G. ; Vasoli, V. (2001), Large amplitude perturbations in mesospheric OH Meinel and 87-km Na lidar temperatures around the autumnal equinox, *Geophys. Res. Lett., 28(9),* 1899 (2000GL012682)

Taylor, M.J.; Taori, A.K.; Hatch, D.R.; Liu, H.L.; Roble, R.G. (2005), Characterization of the semi-annual-oscillation in mesospheric temperatures at low-latitudes, *Adv. Space Res., 2005, 35(11),* 2037-43.

Vincent, R.A., S. Kovalam, D.C. Fritts, J.R. Isler (1998), Long-term MF radar observations of solar tides in the low-latitude mesosphere: Interannual variability and comparisons with the GSWM, *J. Geophys. Res., 103 (D8),* 8667-8683.

Walterscheid, R.L.; Schubert, G. (1995), Dynamical-chemical model of fluctuations in the OH airglow driven by migrating tides, stationary tides, and planetary waves, *J. Geophys. Res., 100 (A9),* 17443-9.

Walterscheid, R.L.; Hecht, J.H.; Vincent, R.A.; Reid, I.M.; Woithe, J.; Hickey, M.P. (1999), Analysis and interpretation of airglow and radar observations of quasi-

monochromatic gravity waves in the upper mesosphere and lower thermosphere over Adelaide, Australia (35°S, 138°E), *J. Atm. and Solar-Terr. Phys., 61(6),* 461-78.

Walterscheid, R. L., G. G. Sivjee, and R. G. Roble (2000), Mesospheric and lower thermospheric manifestations of a stratospheric warming event over Eureka, Canada (80°N), *Geophys. Res. Lett., 27*, 2897–2900.

Walterscheid, R. L., S. V. Venkateswaran (1979), Influence of Mean Zonal Motion and Meridional Temperature Gradients on the Solar Semidiurnal Tide: A Spectral Study, Part II. Numerical Results, *J. Atmos. Sci., 36,* 1636-1662.

Weins, R.H., G. Weill (1973), Diurnal, annual and solar cycle variations of the hydroxyl and sodium nightglow intensities in the Europe-Africa sector, *Planet. Space Sci., 21,* 1011-1027.

Zhang, X., J. M. Forbes, M. E. Hagan, J. M. Russell III, S. E. Palo, C. J. Mertens, and M. G. Mlynczak (2006), Monthly tidal temperatures 20–120 km from TIMED/SABER, *J. Geophys. Res., 111,* A10S08, doi:10.1029/2005JA011504.

Table 1. Annual and semiannual oscillation characteristics for OH and O2 emission temperatures and intensities at low latitude sites. Alice Springs data are fits to monthly averages taken from 11-18 UT; local midnight is at 14:30 UT. Results from the TIME-GCM model at Alice Springs (23 S) are averaged in a similar manner, and are shown in italics. TIME-GCM intensities are scaled to the mean value of the observed intensity.

[a] Clemesha et al., (1990), 1983-1986, [b] Takahashi et al., (1995), 1987-1991,[c] Shepherd et al., (2004)

Quantity and location		**Annual**		**Semi-annual**	
OH temperature	**Mean T (K)**	**Amplitude (K)**	**Phase (days)**	**Amplitude (K)**	**Phase (days)**
Alice Springs (23°S, 133°E) OH (6,2)	194.8 +/-0.4	0.1 +/-0.5	191 +/-287	3.9 +/-0.5	84 +/-4
Alice Springs (23°S, 133°E) OH (6,2) (TIME-GCM)	*183.7 +/-0.1*	*0.7 +/-0.2*	*340 +/-20*	*5.5 +/-0.2*	*90 +/-1*
[a] Cachoeira Paulista (23S, 45W), OH (9,4)	192.8	2.3	84	3.0	91
[b] Cachoeira Paulista (23S, 45W), OH (9,4)	201	0.3	183	3.5	100
[c] WINDII, 87 km (25 S)	194.3	4.2	205	2.4	124
O2A Temperature					
Alice Springs (23°S, 133°E) O2 (0,1)	182.7 +/- 0.2	0.02 +/- 0.23	113 +/- 365	3.8 +/-0.5	114 +/-3
Alice Springs (23°S, 133°E) O2 (0,0) (TIME-GCM)	*184.3 +/-0.2*	*2.2 +/-0.2*	*331 +/-6*	*4.3 +/-0.2*	*90 +/-1*
[a] Cachoeira Paulista (23S, 45W), O2 (0,1)	197.7	2.5	131	2.2	47
OH intensity	**Mean I (R)**	**Amplitude (%)**	**Phase (days)**	**Amplitude (%)**	**Phase (days)**
Alice Springs (23°S, 133°E) OH (6,2)	1236 +/-10	13.9 +/-1.2	206 +/-4	7.0 +/-1.2	112 +/-4
Alice Springs (23°S, 133°E) OH (6,2) (TIME-GCM)		*4.1 +/-0.5*	*289 +/-6*	*5.9 +/-0.5*	*98 +/-2*
O2 intensity					
Alice Springs (23°S, 133°E) O2 (0,1)	224.5 +/-3.2	7.6 +/-1.8	11 +/-16	29.4 +/-2.0	105 +/-2
Alice Springs (23°S, 133°E) O2 (0,0) (TIME-GCM)		*8.6 +/-0.7*	*155 +/-3*	*11.4 +/-0.9*	*85 +/-2*

Table 2. Annual and semiannual oscillation characteristics for OH and O2 emission temperatures and intensities at mid-latitude sites. Results from the TIME-GCM model at Adelaide are shown in italics. TIME-GCM intensities are scaled to the mean value of the measured intensity.

[a]Lopez-Gonzalez (2004), [b] Shepherd et al., (2004),[c] Reid and Woithe, (2007)

		Annual		Semi-annual	
OH temperature	**Mean T (K)**	**Amplitude (K)**	**Phase (days)**	**Amplitude (K [%])**	**Phase (days)**
Adelaide (34°S, 138° E) OH (6,2)	189.2 +/-0.3	10.2 +/-0.4	213 +/-2	3.0 +/-0.5	22 +/-4
Adelaide (34°S, 138°E) OH (6,2) (TIME-GCM)	*188.1 +/-0.1*	*9.1 +/-0.2*	*184 +/-1*	*2.6 +/-.2*	*94 +/-2*
[c] Adelaide FTIR OH (6,2)	192	7.2	187	2.8	106
[a] Sierra Nevada (37N, 3W) OH (6,2)	202	14	8	3	79
[b] WINDII, 87 km (35 S)	192.0	5.8	151	1.8	119
O2A Temperature					
Adelaide (34°S, 138° E) O2 (0,1)	186.4 +/-0.3	2.6 +/-0.5	221 +/-10	4.7 +/-0.4	92 +/-3
Adelaide (34°S, 138°E) O2 (0,0) (TIME-GCM)	*188.9 +/-0.2*	*3.6 +/-0.2*	*206 +/-4*	*2.2 +/-.2*	*84 +/-3*
[a] Sierra Nevada (37N, 3W) O2 (0,1)	190	9	8	5	73
[c] Adelaide FTIR O2 (0,1)	201	1.9	76	7.4	124
OH intensity	**Mean I (R)**	**Amplitude (%)**	**Phase (days)**	**Amplitude (%)**	**Phase (days)**
Adelaide (34°S, 138° E) OH (6,2)	1142 +/-11	17.3 +/-1.3	174 +/-4	3.3 +/-1.3	134 +/-11
Adelaide (34°S, 138°E) OH (6,2) (TIME-GCM)		*6.1 +/-0.7*	*265 +/-6*	*6.8 +/-0.7*	*177 +/-3*
[a] Sierra Nevada (37N, 3W) OH (0,1)	690	13.0	2	11.5	27
O2 intensity					
Adelaide (34°S, 138° E) O2 (0,1)	152 +/-2	6.9 +/-2.0	31 +/-20	28.6 +/-2.3	111 +/-2
Adelaide (34°S, 138°E) O2 (0,0) (TIME-GCM)		*3.1 +/-0.9*	*308 +/-17*	*5.9 +/-0.9*	*18 +/-4*
[a] Sierra Nevada (37N, 3W) O2 (0,1)	380	13.1	42	15.8	53

Table 3. Summary of OH emission temperature and intensity features at both sites. The temporal agreement between the data and model is shown in bold (complete agreement) or italics (phase difference between data and model), significant amplitude differences between the data and model are indicated by underlining, and observed features completely absent from the model are shown in plain type.

	Alice Springs OH Temperature	Adelaide OH Temperature	Alice Springs OH Intensity	Adelaide OH Intensity
Summer Solstice (January)	**Minimum, 12 UT**	*Minimum, 12 UT*	**Minimum, 14:30 UT**	**Minimum, 14:30 UT, March**
Winter Solstice (June/July)	*Minimum, 16 UT*	**Weak min, 13 UT**	Max, 11 UT, **Min, 18UT**	Max, 11 UT **Min, 14:30 UT**
Equinox	**Maximum, 18 UT**	**Maximum, 18 UT**	**Maximum, 11 UT**	*Maximum, 18 UT*
Equinox			**Maximum, 18 UT, October**	**Maximum, 11 UT**
2002 Stratospheric Warming	**Stronger equinoctial max, weaker solstice min**	**Stronger equinoctial max, weaker solstice min**	None significant	**Weaker equinox max, 11 UT**

Table 4. Summary of O2 emission temperature and intensity features at both sites. The temporal agreement between the data and model is shown in bold (complete agreement) or italics (phase difference between data and model), significant amplitude differences between the data and model are indicated by underlining, and observed features completely absent from the model are shown in plain type.

	Alice Springs O2 Temperature	Adelaide O2 Temperature	Alice Springs O2 Intensity	Adelaide O2 Intensity
Summer Solstice (January)	**Minimum, 11 UT**	**Minimum, 11 UT**	**Minimum, pre-midnight**	Minimum, 14 UT
Winter Solstice (June/July)	*Minimum, 16 UT*	**Minimum, Pre-midnight**	*Minimum, 18 UT*	*Minimum, 14 UT*
Equinox	**Maximum, 18 UT**	**Maximum, 18 UT**	**Maximum, 18 UT equinoxes**	**Maximum, Most of night, April**
2002 Stratospheric Warming	None significant	**Strong equinoctial max, April, Oct.**	**Stronger max, October**	Weaker winter min, **strong Oct. max**

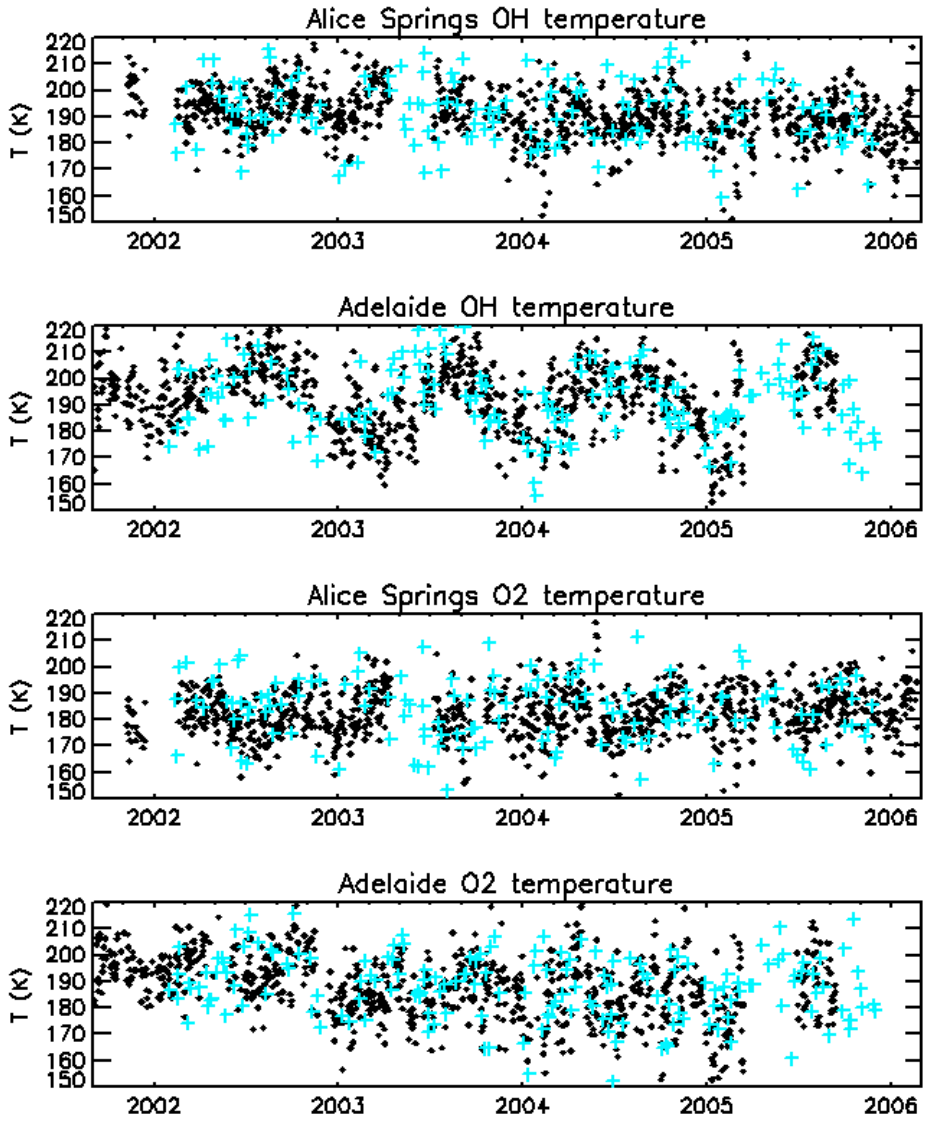

Figure 1. Nightly mean temperature of OH and O_2 atmospheric emissions at Alice Springs (top panels) and Adelaide (bottom panels). Blue crosses are SABER overpass data used in calibration.

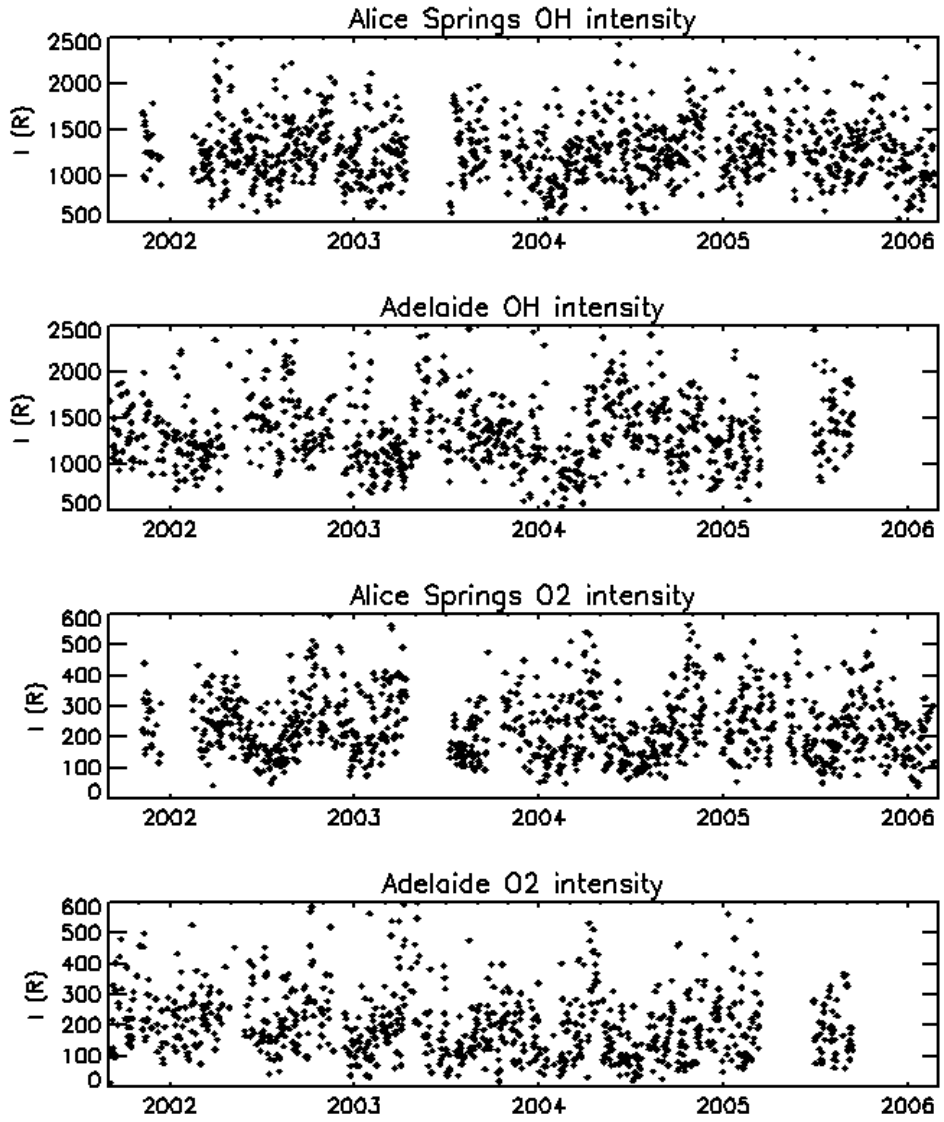

Figure 2. Nightly mean intensity of OH and O_2 atmospheric emissions at Alice Springs and Adelaide. Blue crosses indicate SABER overpass data used in calibration.

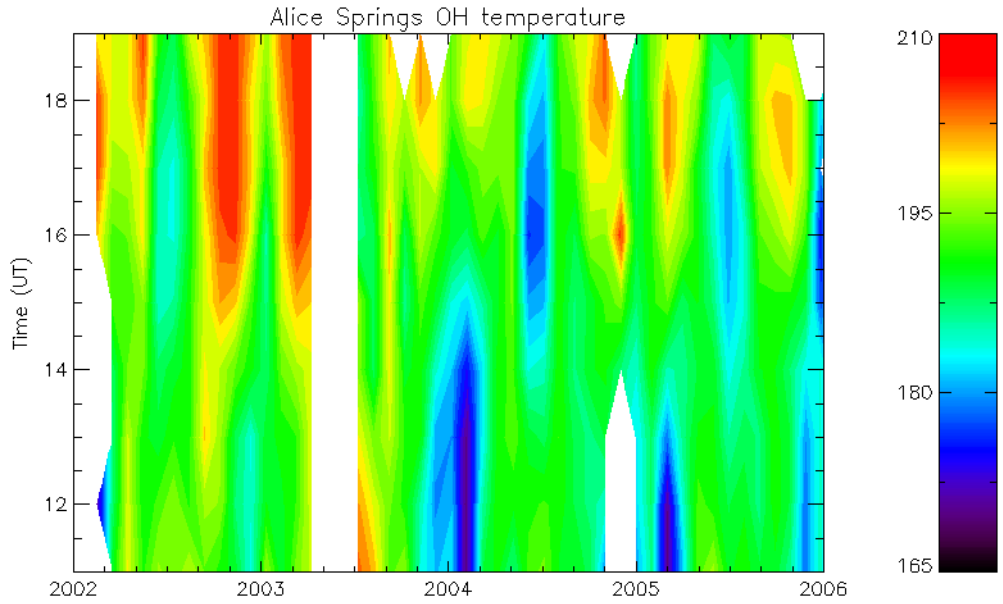

Figure 3. Observed Alice Springs OH emission temperature shown as a function of day-of-year and local time.

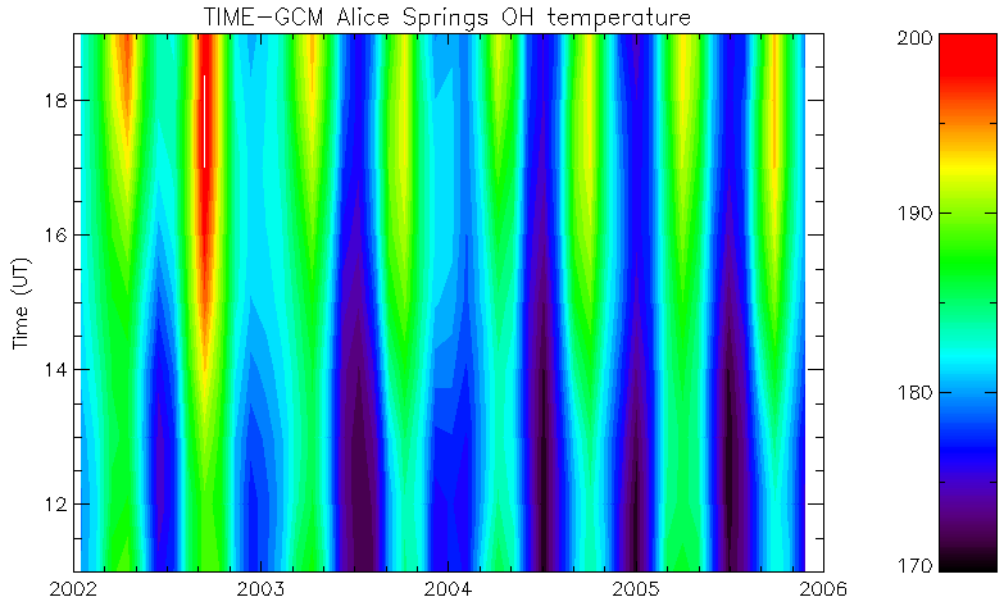

Figure 4. Alice Springs OH emission temperature determined from TIME-GCM shown as a function of day-of-year and local time.

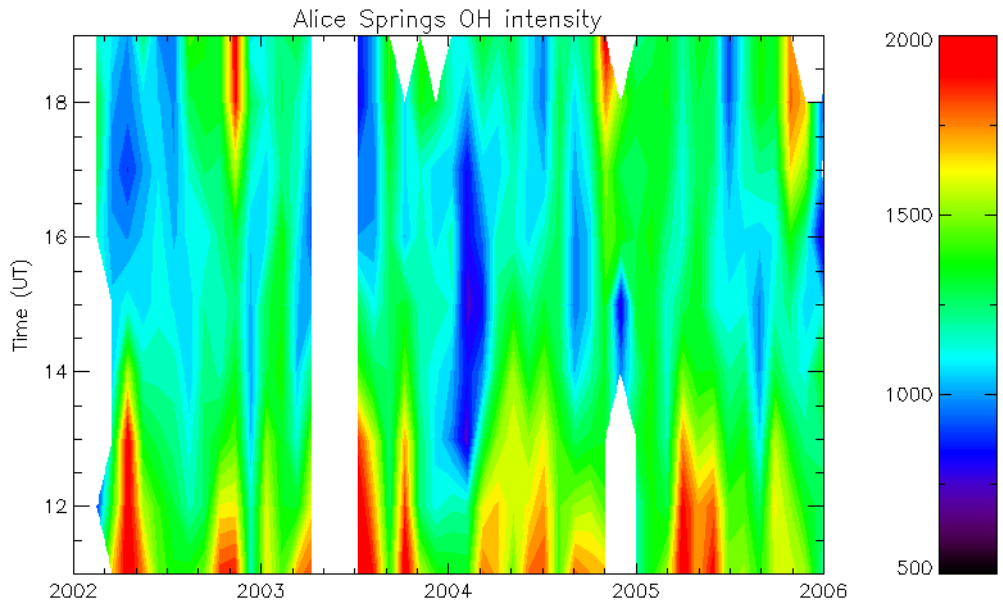

Figure 5. Observed Alice Springs OH emission intensity shown as a function of day-of-year and local time.

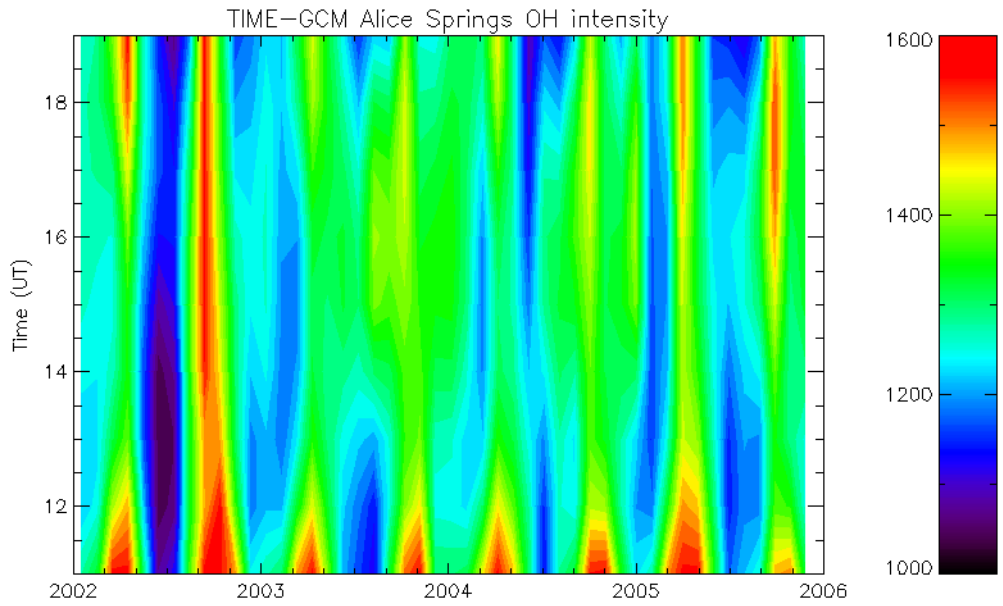

Figure 6. Alice Springs OH emission intensity determined by TIME-GCM shown as a function of day-of-year and local time.

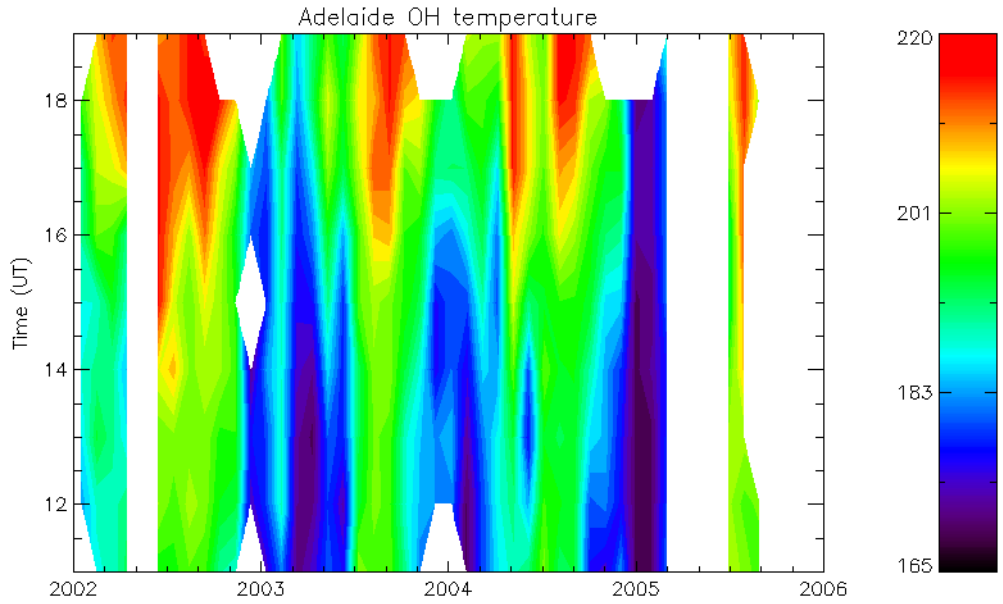

Figure 7. Observed Adelaide OH emission temperature shown as a function of day-of-year and local time.

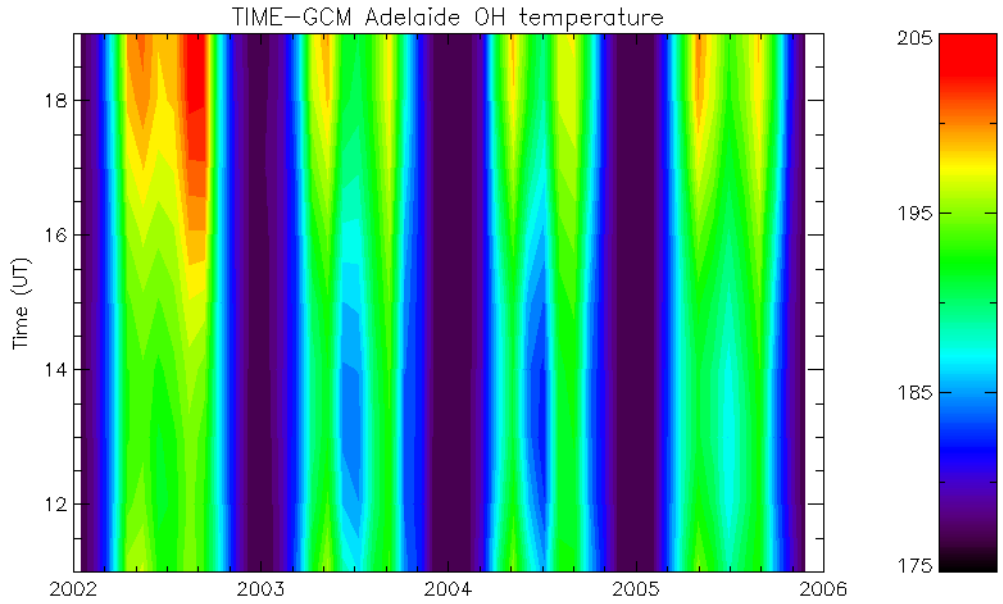

Figure 8. Adelaide OH emission temperature determined from TIME-GCM shown as a function of day-of-year and local time.

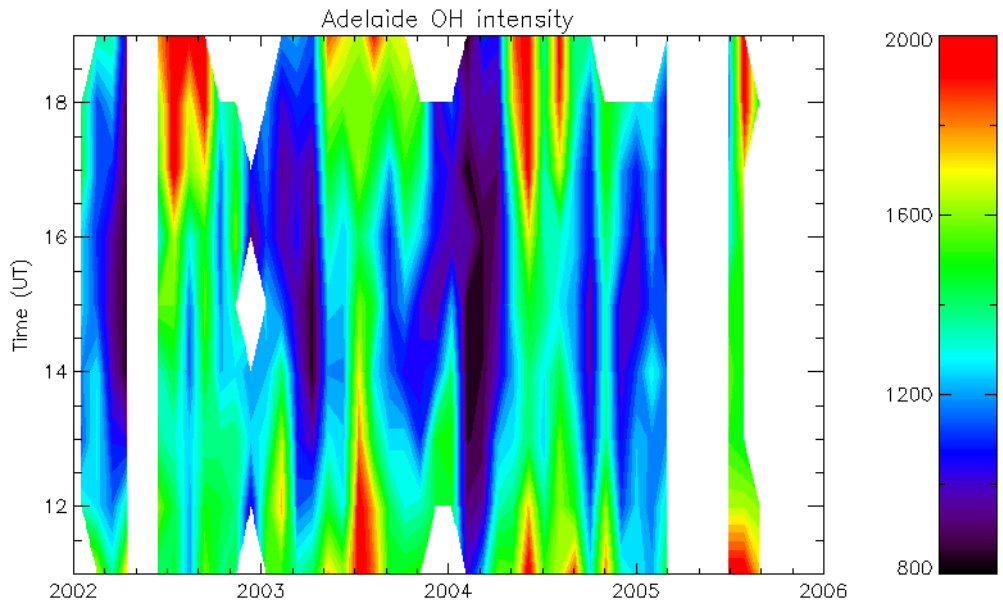

Figure 9. Observed Adelaide OH emission intensity shown as a function of day-of-year and local time.

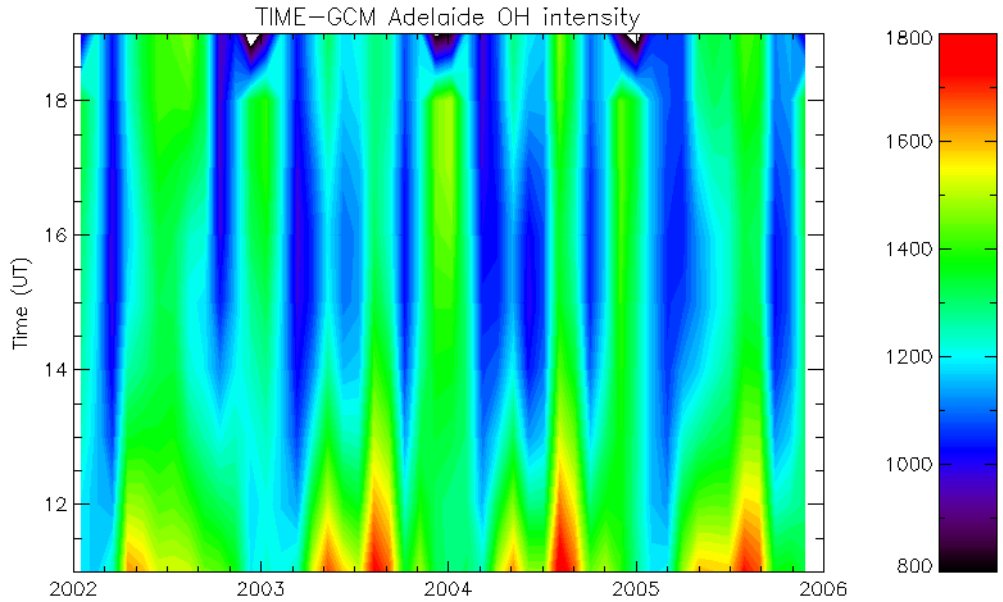

Figure 10. Adelaide OH emission intensity determined by TIME-GCM shown as a function of day-of-year and local time.

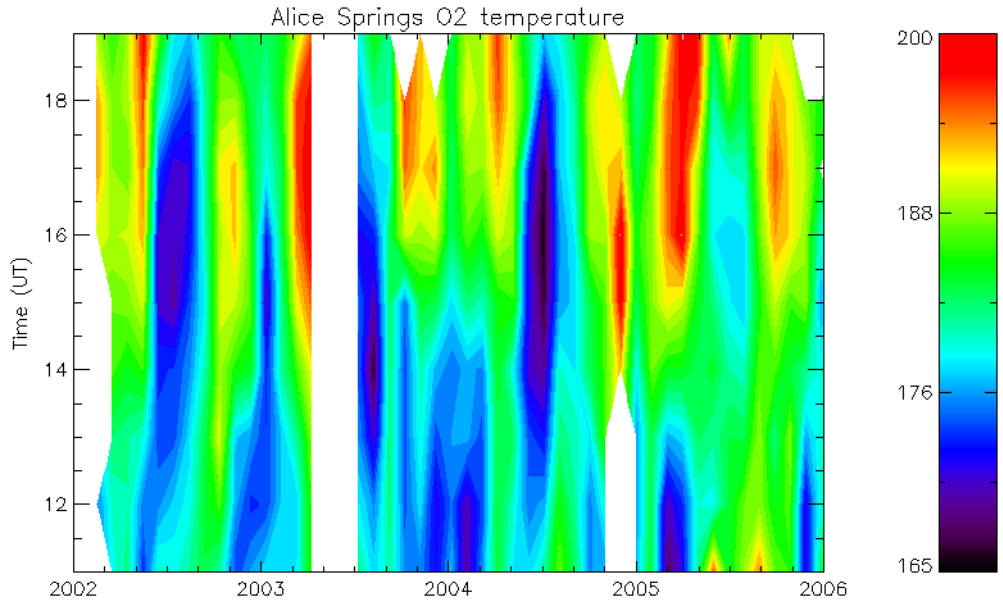

Figure 11. Observed Alice Springs O2A emission temperature shown as a function of day-of-year and local time.

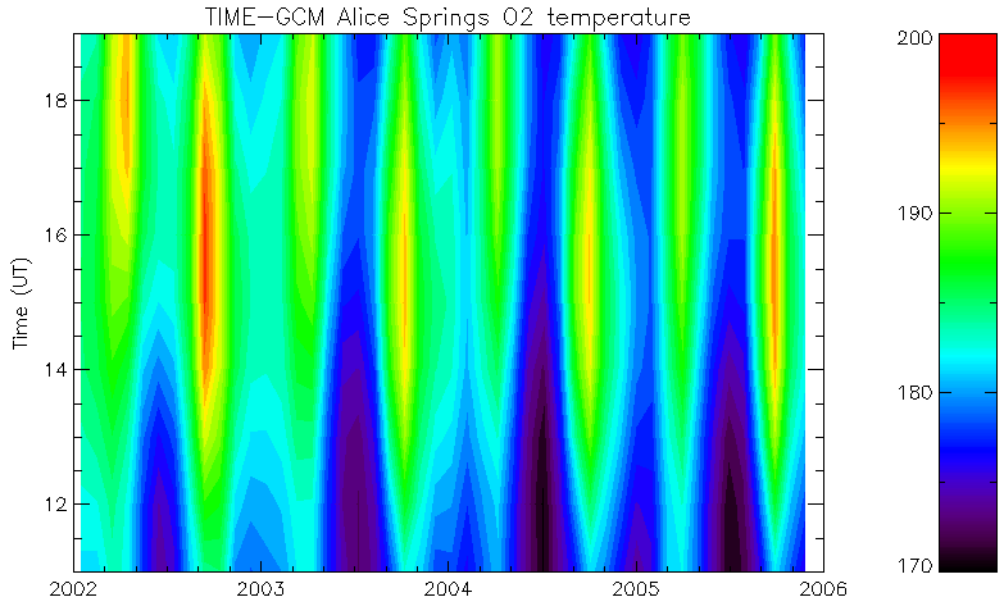

Figure 12. Alice Springs O2A emission temperature determined by TIME-GCM shown as a function of day-of-year and local time.

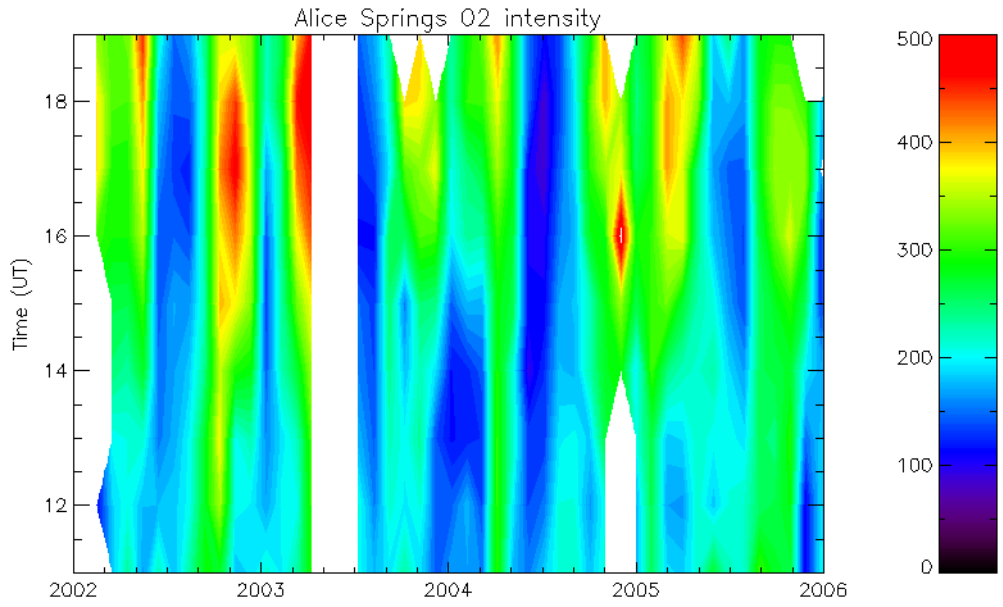

Figure 13. Observed Alice Springs O2A emission intensity shown as a function of day-of-year and local time.

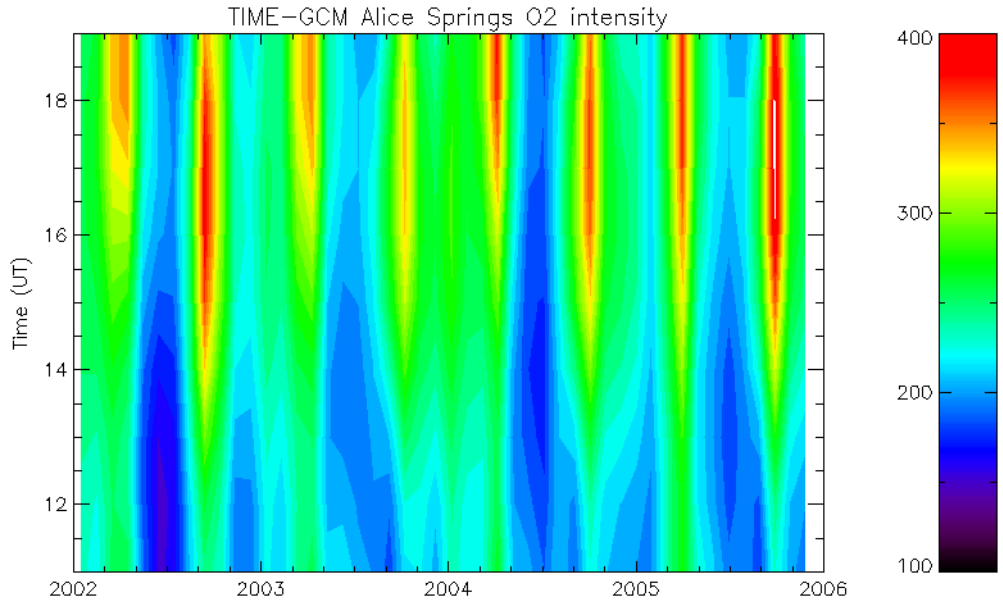

Figure 14. Alice Springs O2A emission intensity determined by TIME-GCM shown as a function of day-of-year and local time.

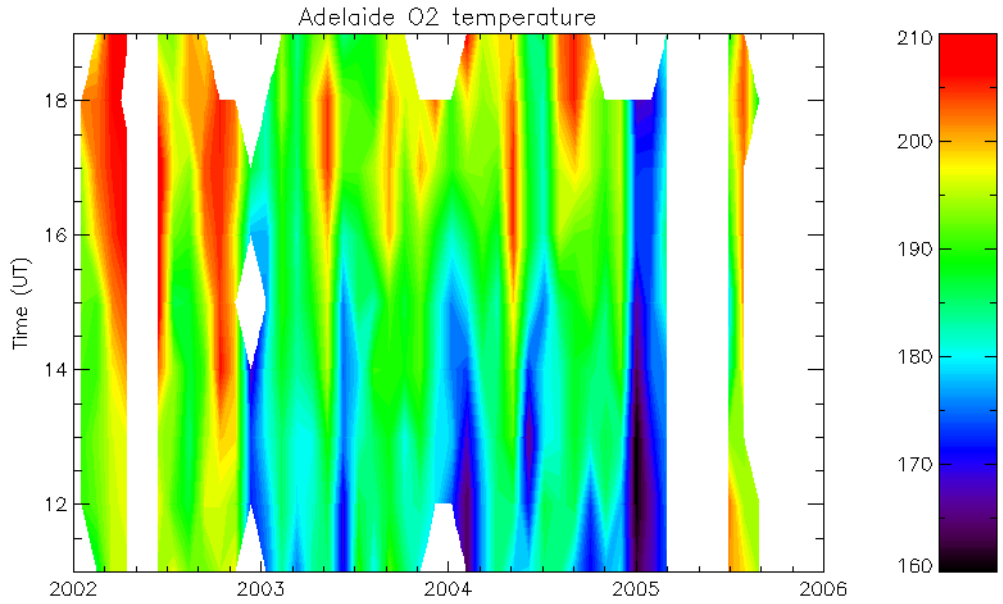

Figure 15. Observed Adelaide O2A emission temperature shown as a function of day-of-year and local time.

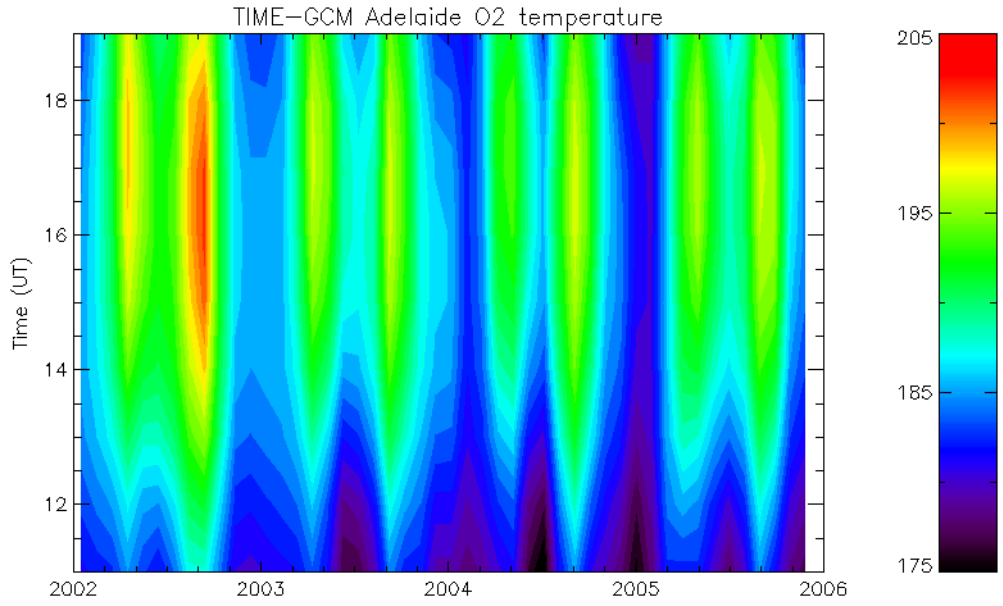

Figure 16. Adelaide O2A emission temperature determined by TIME-GCM shown as a function of day-of-year and local time.

1

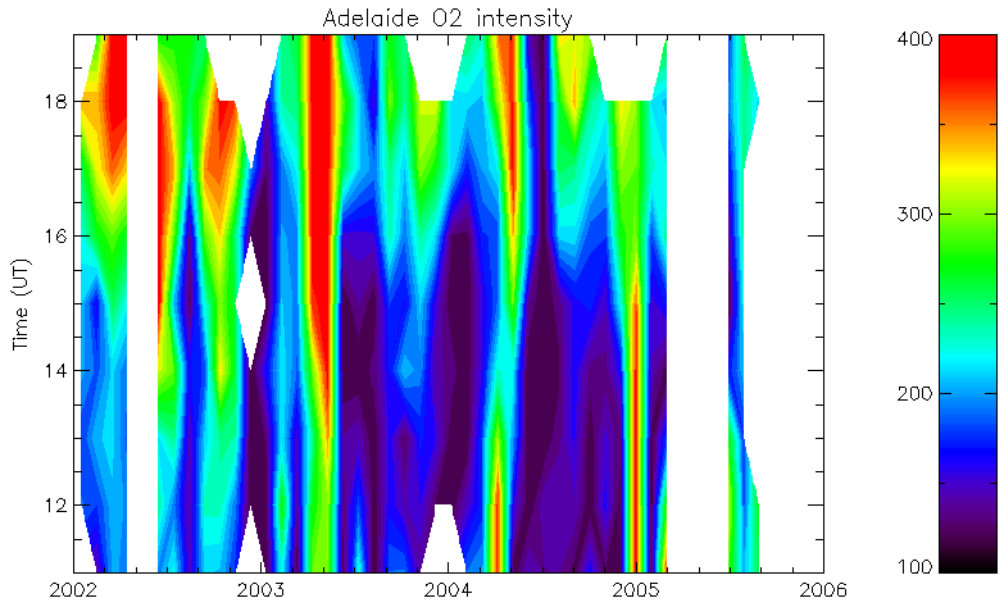

2

3 **Figure 17. Observed Adelaide O2A emission intensity shown as a function of day-of-year and local**
4 **time.**

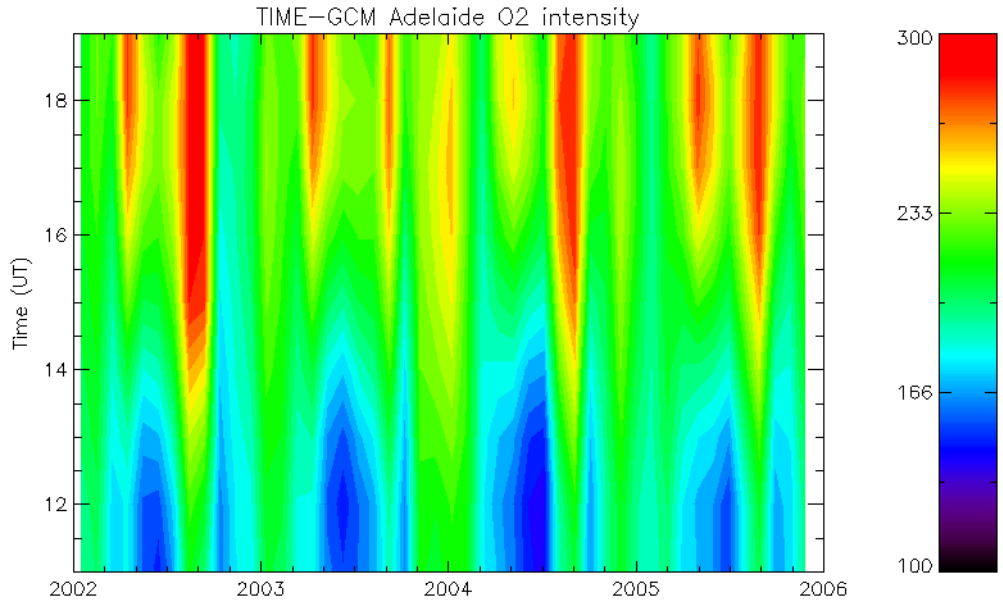

Figure 18. Adelaide O2A emission intensity determined by TIME-GCM shown as a function of day-of-year and local time.

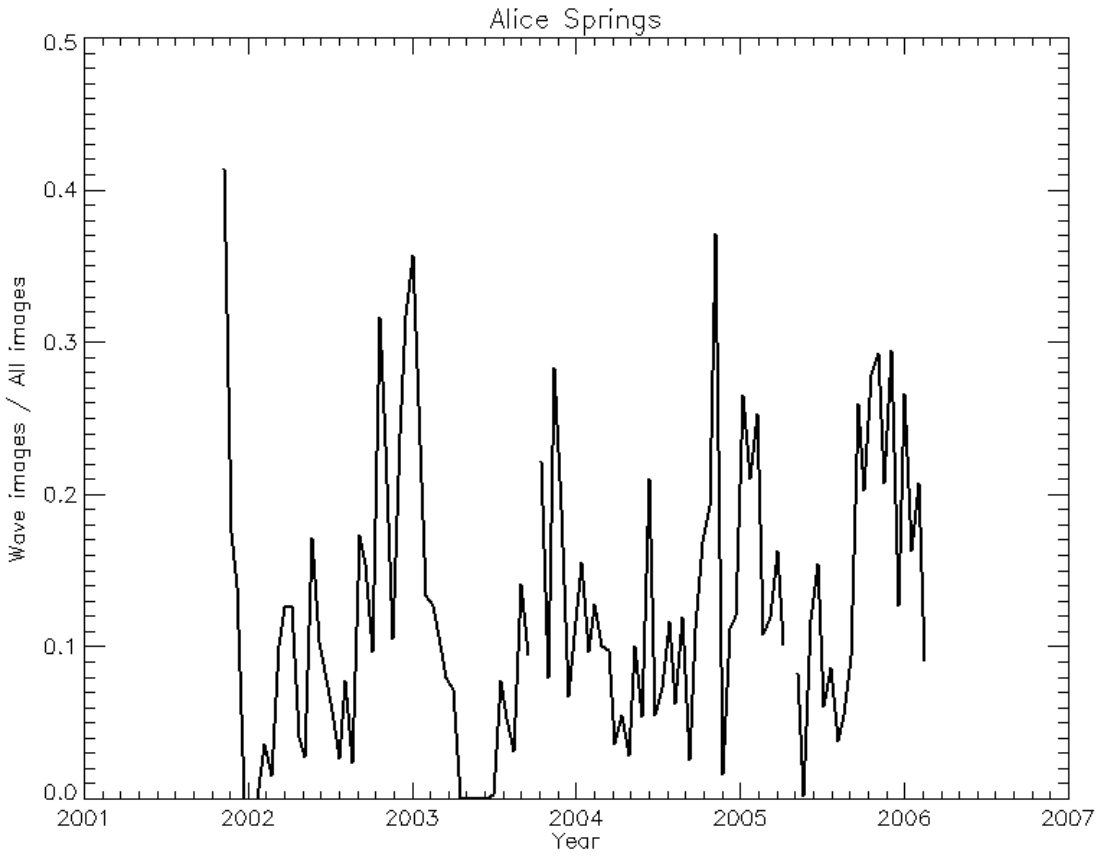

Figure 19. Gravity wave variance in OH emission data at Alice Springs.

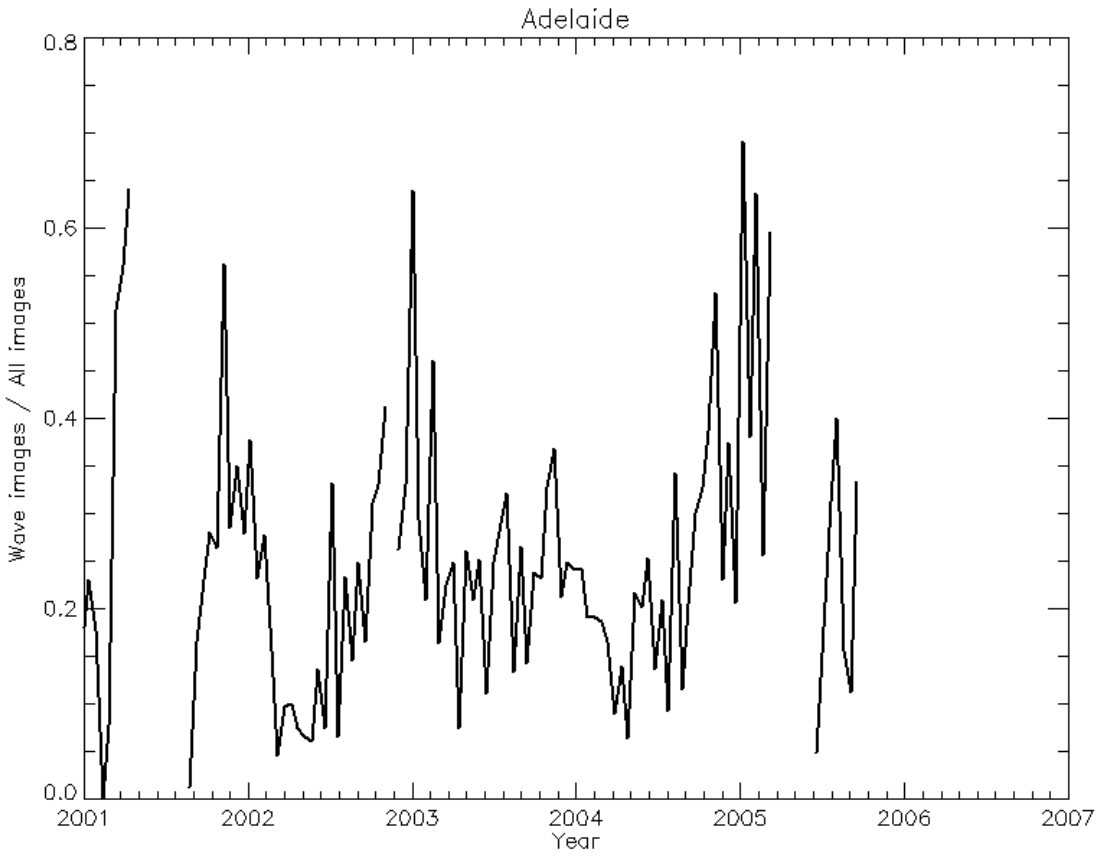

Figure 20. Gravity wave flux determined by OH emission variance at Adelaide.

1
2